A review on the crystalline silicon bottom cell for monolithic perovskite/silicon tandem solar cells

Yan, L. L.; Han, C.; Shi, B; Zhao, Y.; Zhang, X.D.

DOI
10.1016/j.mtnano.2019.100045

Publication date
2019

Document Version
Final published version

Published in
Materials Today Nano

Citation (APA)
Yan, L. L., Han, C., Shi, B., Zhao, Y., & Zhang, X. D. (2019). A review on the crystalline silicon bottom cell for monolithic perovskite/silicon tandem solar cells. *Materials Today Nano*, *7*, 1-13. Article 100045. https://doi.org/10.1016/j.mtnano.2019.100045

Materials Today Nano 7 (2019) 100045

Contents lists available at ScienceDirect

Materials Today Nano

journal homepage: https://www.evise.com/profile/#/MTNANO/login

A review on the crystalline silicon bottom cell for monolithic perovskite/silicon tandem solar cells

L.L. Yan [a, b, c, d], C. Han [a, b, c, d, e], B. Shi [a, b, c, d], Y. Zhao [a, b, c, d, **], X.D. Zhang [a, b, c, d, *]

[a] Institute of Photoelectronic Thin Film Devices and Technology of Nankai University, Tianjin, 300350, China
[b] Key Laboratory of Photoelectronic Thin Film Devices and Technology of Tianjin, Tianjin, 300350, China
[c] Collaborative Innovation Center of Chemical Science and Engineering (Tianjin), Tianjin, 300072, China
[d] Renewable Energy Conversion and Storage Center of Nankai University, Tianjin, 300071, China
[e] PVMD group, Delft University of Technology, Mekelweg 4, 2628 CD Delft, The Netherlands

ARTICLE INFO

Article history:
Received 4 May 2019
Received in revised form
20 June 2019
Accepted 30 June 2019
Available online 13 July 2019

Keywords:
Crystalline silicon solar cell
Perovskite/silicon tandem
Homojunction
Heterojunction

ABSTRACT

Perovskite/silicon tandem solar cells have reached certified efficiencies of 28% (on 1 cm^2 by Oxford PV) in just about 4 years, mostly driven by the optimized design in the perovskite top cell and crystalline silicon (c-Si) bottom cell. In this review, we focus on the structural adjustment of the bottom cell based on the structural evolution of monolithic perovskite/silicon tandem solar cells to improve their performance. To begin with, c-Si solar cells are classified into silicon homojunction and silicon heterojunction (SHJ) devices according to temperature tolerance, and the corresponding structural features are presented. Then, the evolution of monolithic perovskite/silicon tandem cells based on c-Si homojunction and heterojunction bottom devices is summarized. An appropriate candidate of the c-Si bottom cell for monolithic perovskite/silicon tandem cells is proposed, mainly including passivated emitter and rear cell devices, the tunnel oxide passivated contact cell, and SHJ devices. In brief, our review will emphasize the important role of the c-Si bottom cell with different passivation structures for perovskite/silicon tandem cells, which provides a guidance to enhance the performance of tandem cells.

1. Introduction

Solar energy will become a promising alternative to conventional fossil fuel resources in the future owing to its renewability and sustainability [1]. One of the most important utilization approaches is photovoltaic (PV) technology, which directly converts solar energy into electricity [2]. Improving the efficiency of solar cells is one of the technical keys to reduce the cost of PV power generation and simultaneously increase their competitiveness with conventional resources of electricity [3,4]. The most straightforward way is to fabricate multijunction tandem solar cells, which consist of multiple absorption layers with complementary bandgaps [5,6].

The tandem cell concept has been implemented commercially for different absorbers, ranging from the relatively low-cost hydrogenated amorphous silicon (a-Si:H) to the high-performance III-V group materials; a-Si:H with a high absorption coefficient [7], as ultrathin absorbers (hundreds of nanometers), is capable of harvesting photons within the spectral range allowed by the bandgap, which has been considered as excellent candidate materials for fabricating low-cost PV devices [8,9]. However, there is unavoidable Staebler-Wronski Effect [10] limiting its stability under light exposure, resulting from the generation of deep defects that act as recombination centers [11,12]. Although III-V multijunction solar cells have demonstrated a power conversion efficiency (PCE) in excess of 30% [13], such as triple-junction InGaP/GaAs/InGaAs solar cells with a PCE of 37.9% [14], the complicated and costly manufacturing processes [15,16] limit their extensive applications, such as space [17] or concentrator PVs [18]. Therefore, it is very important to design and implement a tandem solar cell with both low cost and high efficiency.

Compared with other PV materials, crystalline silicon (c-Si) with an energy bandgap of 1.12 eV is one of the most appropriate

---

* Corresponding author. Institute of Photoelectronic Thin Film Devices and Technology of Nankai University, Tianjin, 300350, China.

** Corresponding author. Institute of Photoelectronic Thin Film Devices and Technology of Nankai University, Tianjin, 300350, China.

E-mail addresses: zhaoygds@nankai.edu.cn (Y. Zhao), xdzhang@nankai.edu.cn (X.D. Zhang).

https://doi.org/10.1016/j.mtnano.2019.100045
2588-8420/

candidates for building multijunction cells owing to its suitable bandgap, high efficiency, cost competitiveness, non-toxicity, and good stability [19]. Since the first silicon solar cell with a PCE of around 4.5% in the early 1950s was successfully realized in Bell Labs [20], the efficiency of c-Si solar cells has been improved to the current record of 26.6% [21], approaching their theoretical Auger efficiency limit of 29.4% [22]. As a result, c-Si cells are nearly ideal in the role of the low bandgap bottom cell. Recently, organic-inorganic lead halide perovskite solar cells (PSCs) have made remarkable progress and exhibited a high PCE up to 24.2% at the single-junction level [23] owing to the advantages such as strong optical absorption [24] and long diffusion lengths [25]. In addition, a steep absorption edge [24] and tunable bandgap of 1.5–1.8 eV [26] can be obtained in PSCs, which makes them an attractive top cell candidate for tandem devices [27]. Inspiringly, perovskite/silicon tandem cells are expected to have an efficiency potential beyond 30% at low manufacturing costs [28–30].

Generally speaking, as shown in Fig. 1, there are mainly the mechanically stacked four-terminal (4T) and monolithically integrated two-terminal (2T) tandem devices [31]. In the simple 4T configuration in Fig. 1(a), two independent subcells with different bandgaps are fabricated, which are electrically isolated from each other, and the output power is extracted separately [32,33]. This structure has obvious advantages of process simplicity, allowing for independent optimization of the subcells without any additional processing restrictions [34]. Unfortunately, it requires more functional materials, such as substrates and transparent conductive oxides (TCOs) [35–37]. Other 4T tandem concepts were also realized, such as spectral splitting systems [38] or reflective tandems [39]. Fig. 1(b) presents the most desirable 2T configuration, in which the top cell is directly deposited onto the bottom cell. Compared with the 4T configuration, the monolithic 2T configuration contains the minimum number of functional layers, resulting in the potential for low cost and low optical and electrical losses [40,41]. Moreover, being more easily integrated in a PV system, the 2T design requires only one junction box, whereas the 4T tandem would need two. However, the two subcells of the 2T tandem should be designed to generate similar photocurrent in both subcells, the so-called ‘current matching.’ For example, adjusting the perovskite absorber thickness, improving the infrared spectral response, and decreasing the reflection losses and parasitic absorption [42,43] are effective approaches to achieve current matching. And an interface layer (TCO or a thin silicon film) is required for all demonstrated monolithically integrated perovskite/silicon tandems for electrical connection between the top and the bottom cells. The interfacial layer is supposed to present less parasitic absorption at wavelengths above 800 nm and sufficient vertical conductivity while exhibiting low lateral conductivity. Finally, in the 2T tandem, generally, c-Si solar cells are processed with a flat front side to be compatible with the spin-coating perovskite layer because the perovskite layer with a thickness of 200–600 nm via spin coating is difficult to be conformal on the texturing surface with 1–10-μm pyramids, so the thermal evaporation method to prepare the perovskite layer on the textured surface was demonstrated [43]. From the aforementioned information, the monolithic 2T devices arguably have the highest potential to reach a low levelized cost of electricity.

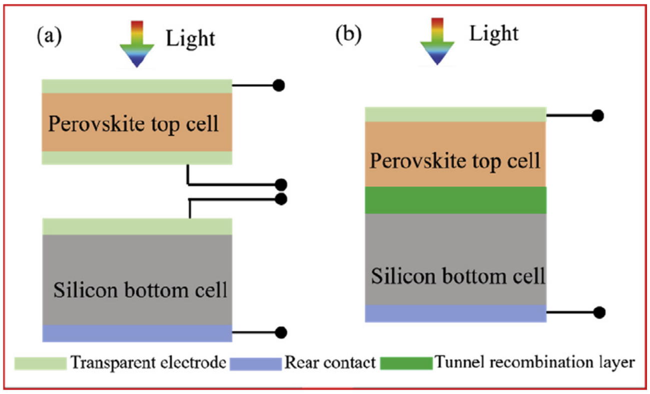

Fig. 1. Schematics of the perovskite/silicon tandem configuration: (a) mechanically four-terminal (4T) and (b) monolithically two-terminal (2T).

There are two kinds of monolithic perovskite/silicon tandem cells, perovskite/homojunction and perovskite/heterojunction. Higher temperature tolerance (>400 °C) makes c-Si homojunction bottom cells compatible with the commonly used titanium oxide (TiO_x) electron transport layers in the top mesoporous perovskite cell. Limited by the thermal stability of intrinsic a-Si:H passivation layers for silicon heterojunction (SHJ) cells, a planar perovskite top cell with an electron-selective contact processed at low temperatures is one suitable option to solve this problem, namely, the available structure of the top perovskite cell is directly determined by the c-Si bottom cell. Therefore, making a comprehensive study of the c-Si bottom cell becomes increasingly important to integrate the appropriate PSCs. Here, we first give a detailed introduction for c-Si homojunction and SHJ devices. The former group mainly includes passivated emitter and rear cell (PERC) devices, passivated emitter and rear locally diffused (PERL) cells, passivated emitter and rear totally diffused (PERT) cells, and the tunnel oxide passivated contact (TOPCon) cell. After that, the structural evolution of c-Si–based tandem devices is presented in detail. Finally, the PCE of tandem cells is predicted based on the state of the art in the c-Si homojunction and SHJ bottom cells.

2. Classification of c-Si bottom cells for 2T perovskite/silicon tandem cells

For monolithic tandem cells, process compatibility comes first, namely, the high temperature tolerance of the c-Si bottom cell should be taken into full consideration when the perovskite top cell is prepared. In this section, c-Si bottom cells for tandem cells are categorized as homojunction (high temperature tolerance >400 °C) and heterojunction solar cells (low temperature tolerance<250 °C). The band diagram of homojunction and heterojunction c-Si cells is shown in Fig. 2. Compared with the band diagram of homojunction cells in Fig. 2(a) [44], the performance of heterojunction solar cells, shown in Fig. 2(b), is influenced by the asymmetry between conduction and valence band offsets (ΔE_C, ΔE_V) [45–48].

2.1. Silicon homojunction solar cells

The most widespread industrial fabrication method for silicon homojunction solar cells will be described in the following section first, including PERC devices and PERL and PERT cells, collectively known as the PERX group. After that, the TOPCon structure with an ultrathin tunnel oxide layer and a doped polycrystalline Si (poly-Si) layer will also be presented in detail.

2.1.1. PERX group

The conventional c-Si cell with full-area aluminum back surface field (Al-BSF) in Fig. 3(a) is still the most common approach in the industrial screen-printed p-type c-Si solar cells [49] owing to its simplicity, low cost, and high reliability. However, the full-area Al-BSF only provides a moderate quality of passivation of the rear surface and has serious limitations of achieving ≥20% efficiencies,

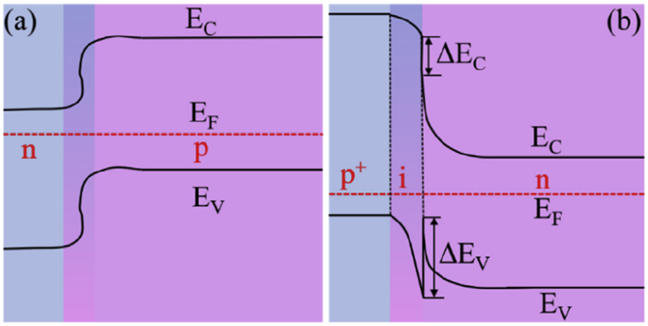

Fig. 2. Schematic band diagram of a silicon cell based on (a) homojunction and (b) heterojunction. E_C, E_V, E_F, ΔE_C, and ΔE_V denote the conduction band edge, the valence band edge, the Fermi level, the conduction band offset, and the valence band offset, respectively. n, p, i, and p^+ are the n-type and the p-type c-Si, the intrinsic and the B-doped a-Si:H films, respectively. c-Si, crystalline silicon.

especially on thinner wafers [50]. To overcome the disadvantages of the full-area Al-BSF cell, a rear dielectric passivation scheme is added to the PERC device, followed by the formation of local Al-BSF, as shown in Fig. 3(b). Therefore, a significant performance enhancement of the PERC device is achieved owing to its reduced back surface recombination velocity and high internal reflection from the passivated rear surface. The PERC devices of 4 cm^2 area fabricated on 0.2 Ω cm, p-type, float-zone (FZ) substrates demonstrated a PCE of 22.8% by Blakers et al. [51] at the University of New South Wales (UNSW) in 1989. In their work, the smaller direct contact area between the rear metal and silicon substrate was further passivated, thus effectively reducing the recombination velocity at the interface. As shown in Table 1, compared with the best full-area Al-BSF devices at that time [52,53], the PERC devices displayed markedly superior V_{oc} with an improvement from 669 mV to 696 mV, as well as an enhanced short-circuit current density (J_{sc}). Unfortunately, the fill factors (*FFs*) were slightly decreased from 82.9% to 81.4% owing to lateral resistance loss in the substrate [51]. To solve this problem, the concept of the PERL cell was further proposed [54]. Obviously, the main difference between the PERL cell in Fig. 3(c) and the PERC device in Fig. 3(b) is the local diffusion of boron in rear contact areas. This reduces the effective recombination rate at the rear contacts by suppressing minority carrier concentrations in these regions. Hence, it is possible to reduce the spacing of the rear contact points to decrease the lateral resistance, improving *FFs*. More encouragingly, a PCE of 24.7% on PERL cells was reported by the UNSW in 1999, which had been the efficiency record of c-Si cells for 15 years [55]. The initial PERL cells fabricated on the magnetically confined Czochralski (MCZ)-grown wafers with a higher resistivity of around 5 Ω cm gave lower *FFs* owing to the current crowding effect [56] resulting from the low coverage, small rear contact areas. Therefore, the PERT structure was first introduced to improve the *FFs* for the high resistivity substrates of 100 Ω cm in the early development stages of the PERL cell [57]. Compared with the PERL cell, as shown in Fig. 3(c), a doped layer is used along the entire rear surface of the PERT device, as shown in Fig. 3(d). In 1999, the PERT cells with a PCE of 24.5% on MCZ substrates were successfully realized by Zhao et al. [55].

Here, the detailed fabrication process of a PERC device is shown in Fig. 4. The fabrication process begins with the double-side alkaline texturing of silicon wafers to form random pyramids. Then, a homogeneous emitter n+ is prepared by diffusion of phosphorus in the standard tube thermal furnace. After diffusion, the phosphorus-silicon glasses are removed by hydrofluoric acid, and the pyramids on the backside of the wafer are etched in alkaline solution to generate a flat surface. Furthermore, a silicon nitride (SiN_x) front antireflective layer and a rear oxide layer are deposited. Then, the rear passivation layer is locally removed by the local ablation process with local contacts. Finally, a screen-printed silver front grid and a screen-printed aluminum on the rear side are applied, followed by a firing step to form a favorable contact of metal-Si.

Obviously, the key point of the PERC device is the deposition of the rear passivation film to reduce surface recombination. There are three kinds of material currently used for surface passivation in the PERC devices, even in the PERX cells. Traditionally, thermally grown silicon dioxide (SiO_2) has been applied as an effective passivation scheme for n- and p-type c-Si, with interface trap densities (D_{it}) below $4 \times 10^9\ cm^{-2}\ eV^{-1}$ [58] and surface recombination velocities below 15 cm/s on 1 Ω cm FZ c-Si [59]. However, high processing temperature (in the range of 950–1,100 °C) and elaborate processing are not always desirable to obtain such high-quality SiO_2,

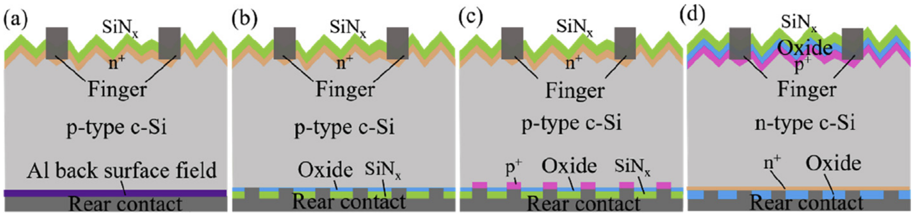

Fig. 3. Schematic view of (a) the standard full-area Al-BSF cell, (b) the PERC device, (c) the PERL cell, and (d) the PERT cell. Al-BSF, aluminum back surface field; PERC, passivated emitter and rear cell; PERL, passivated emitter and rear locally diffused; PERT, passivated emitter and rear totally diffused; c-Si, crystalline silicon.

Table 1
Performance parameters of the 4-cm^2 c-Si cell under the standard global AM1.5 spectrum (100 mW/cm^2) at 25 °C.

Cell structure	Substrate resistivity (Ω. cm) and type	V_{oc} (mV)	J_{sc} (mA/cm^2)	*FF* (%)	PCE (%)
Al-BSF [53]	0.2, p-type, FZ	669	38.6	82.9	21.4
PERC [51]	0.2, p-type, FZ	696	40.3	81.4	22.8
PERL [55]	1.0, p-type, FZ	706	42.2	82.8	24.7
PERT [55]	4.8, p-type, MCZ	704	41.6	83.5	24.5

Al-BSF, aluminum back surface field; *FF*, fill factor; PCE, power conversion efficiency; FZ, float-zone; MCZ, magnetically confined Czochralski; PERC, passivated emitter and rear cell; PERL, passivated emitter and rear locally diffused; PERT, passivated emitter and rear totally diffused; c-Si, crystalline silicon.

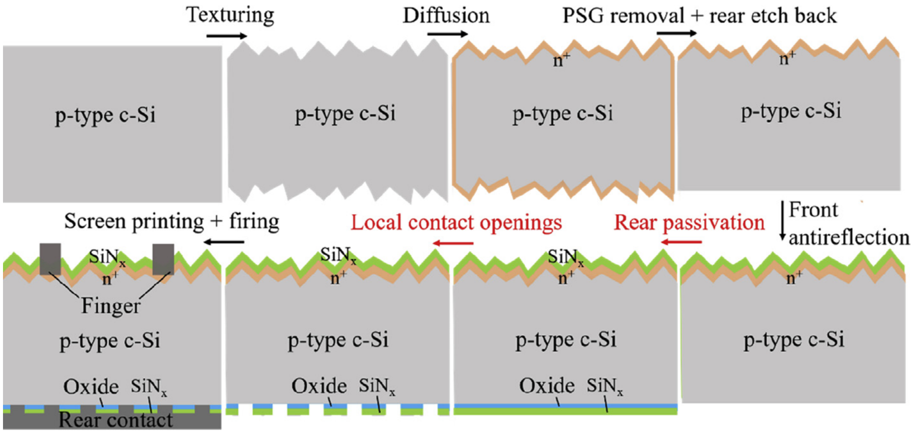

Fig. 4. Fabrication scheme of the PERC device. PSG, phosphorus-silicon glass; PERC, passivated emitter and rear cell; c-Si, crystalline silicon.

and only c-Si with low impurity content such as FZ c-Si can be used without significant bulk lifetime degradation [60]. In addition, silicon nitride (SiN_x) with a positive fixed charge density (~10^{12} cm^{-2}) [61] inducing field-effect passivation is particularly beneficial for passivation of highly doped n-type c-Si because the minority carriers (holes) are effectively shielded from the c-Si surface [62,63]. Hence, SiN_x applied at the rear side of p-type c-Si is not a suitable candidate owing to parasitic shunting [62,63]. Another interesting option is the use of dielectric aluminum oxide (Al_2O_3) with a negative fixed charge (~10^{13} cm^{-2}) [64] by atomic layer deposition (ALD) as a surface passivation layer for the p-type c-Si. Hoex et al. [64] demonstrated that excellent surface passivation of c-Si was achieved by the Al_2O_3 layer, which could yield better results than forming gas annealed thermal SiO_2 and the as-deposited SiN_x layer from comparative experiments [65,66]. In addition, the results of the study by Benick et al. [67] also indicated excellent passivation from Al_2O_3 on highly doped p-type c-Si. Currently, it has been reported that Al_2O_3/SiN_x stack passivation could be an appropriate and cost-effective option for the PV industry. In addition, as another key technique, the local contact openings in a PERC device can be made by laser ablation [68,69] or chemical etching [70] on the dielectric layer of the rear surface before screen printing. Laser ablation is commonly used in industrial PERC fabrication owing to the manageable and repeatable processing [71,72]. Indeed, a compromise between the contact area and finger spacing on the dielectric layer is an essential issue, which has significant impact on contact formation and recombination on the rear surface [73,74]. It has also been established that the rear opening geometry influenced the Kirkendall void formation, and line contacts performed better than point contacts [75,76].

Besides the aforementioned two key technologies in the PERC device, rear localized contacts formed by doping heavily are also important for the PERL cells. Laser-doping techniques appear to be increasing in popularity for the localized contacts of the PERL cell owing to the incorporation of doping and opening [77], namely, laser doping can be integrated into the laser ablation process to open the rear dielectric layer, minimizing the impact on the process steps. For example, Lin et al. [78] found that Kirkendall void formation at the contact regions can be avoided by heavily incorporating boron laser doping on the rear surface of PERL cells, followed by adjusting the firing profile. In the research by Cornagliotti et al, when the dielectric layers were patterned by the laser for local contact, the Al atoms from the Al_2O_3 film were incorporated into the underlying Si bulk. With this technique, they successfully realized substantial dopant incorporation for 10 nm of ALD Al_2O_3, without using additional doping sources [79]. The full-area BSF of a PERT cell and the doping of the emitter need to be developed with a reproducible, damage-free, and high-quality fabrication of the doped areas [80].

Without temperature limitation, it is feasible for the PERX group as bottom connecting with all PSCs owing to high temperature tolerance. But the complex localized contact and/or doped regions technology following moderate quality of passivation increases the cost of tandem cells.

2.1.2. *Tunnel oxide passivated contact cell*

Although highly efficient passivated contacts for solar cells can be achieved by the aforementioned PERX technology with partial rear contacts, the complicated and unavoidable local contact openings may lead to carriers crowding at the opening. As shown in Fig. 5(a), based on 1–2-nm-thick tunnel oxide on c-Si and a phosphorus-doped poly-Si layer on SiO_x, the novel TOPCon cell with a confirmed PCE of 23.0% was first developed by the Fraunhofer Institute for Solar Energy Systems (ISE) in 2013 [81,82], which provides an effective solution to the aforementioned problem [83]. The current PCE record of the TOPCon cell was also held by the Fraunhofer ISE, with a value of 25.7% (V_{oc} = 725 mV, $FF = 83.3\%$, $J_{sc} = 42.5$ mA/cm^2) in 4 cm^2 [84]. As shown in Fig. 5(b), although tunnel oxide layers principally act as a barrier for carrier transport and it was already shown that the oxide's valence band offset to Si ($\Delta E_C = 3.1$ eV, $\Delta E_V = 4.5$ eV) is large [85], electrons can overcome this oxide barrier by means of tunneling (direct or trap-assisted) or via pinholes in the oxide, but the direct tunneling process would be less likely for holes due to the oxide's larger

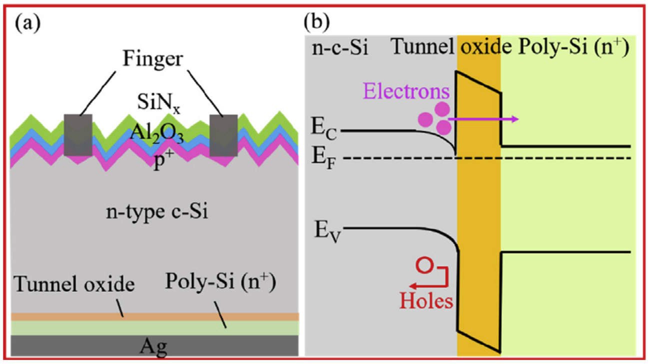

Fig. 5. (a) Sketch of the TOPCon cell structure and (b) schematic band diagram of the TOPCon cell. TOPCon, tunnel oxide passivated contact; c-Si, crystalline silicon.

valence band offset to Si [86]. Additional field-effect passivation is obtained owing to the heavily doped poly-Si layer deposited on the tunneling SiO_x layer.

Generally, an ultrathin tunneling layer of SiO_x can be prepared via wet chemical oxidation with nitric acid [87,88], UV/O_3 [83], or dry thermal oxidation [89]. It should be noted that the performance of a TOPCon cell is sensitive to the thickness of SiO_x films. For instance, Kale et al. [90] demonstrated that on both n- and p-type contacts, there was an optimum thermally grown SiO_x thickness of 1.4–1.6 nm for obtaining the highest implied open-circuit voltage (iV_{oc}) values of ~739 and ~700 mV, respectively. The lower iV_{oc} for contacts with SiO_x<1.4 nm can be attributed to poorer chemical passivation of dangling bonds on the c-Si surface, the inferior passivation quality for contacts with SiO_x>1.6 nm resulted from lesser field-effect passivation [90]. Subsequently, a doped poly-Si film is deposited on SiO_x by either plasma-enhanced chemical vapor deposition (PECVD) [87] or low-pressure chemical vapor deposition [88]. Furthermore, the contacts need to be annealed between 850 and 900 °C after the doped a-Si layer deposition to facilitate crystallization of the as-deposited silicon layer and then reduce the contact resistance for obtaining high iV_{oc} values. Feldmann et al. [81] found that interface passivation decreased owing to local disruption of the SiO_2 tunnel junction in oxygen-free ambient when the annealing temperature was higher than 900 °C. In addition, Rohatgi et al. [91] showed that the higher annealing temperature and the diffusion of more phosphorus dopants are promoted from n^+ poly-Si into the c-Si absorber, which may increase Auger recombination in the bulk and high recombination at the absorber/SiO_x interface. In the work by Tao et al, although tunneling oxide combined with microcrystalline Si (μc-Si):H featured a lower passivation property due to the smaller content of hydrogen than a-Si:H, a lower thermal budget was required to recrystallize, and no blistering was observed for the μc-Si layer [92].

The TOPCon structure with excellent passivated contact enables implementation into a conventional solar cell process and avoids the local contact formation using laser ablation, which is a promising candidate for tandem cells.

2.2. Silicon heterojunction

SHJ solar cells show a high V_{oc} exceeding 750 mV [93], induced by the intrinsic a-Si:H passivation layers on both sides of the c-Si wafer, which is significantly higher than the homojunction cells showing a maximum V_{oc} of around 700 mV. However, the thermal stability of the a-Si:H layer [94] directly limits the top perovskite at low temperature. The structure of low-temperature perovskite consists of regular planar n-i-p and inverted planar p-i-n, leading to the corresponding SHJ bottom cell with the standard front emitter (FE) and rear emitter (RE), as shown in Fig. 6.

2.2.1. Front emitter

Recently, a world record PCE of 25.1% (V_{oc} = 738 ± 0.2 mV, FF = 83.5 ± 0.5%, J_{sc} = 40.8 ± 0.8 mA/cm^2) for the SHJ devices with a FE was reported by reducing carrier recombination at the a-Si/c-Si interface [95], and its typical scheme is shown in Fig. 6(a). Surface texturing enhances light trapping, thanks to multiple reflections, scattering, and extended light paths. And the most widely used textures are random pyramids. The morphology of pyramid geometry is particularly critical to the performance of the textured solar cells, such as pyramidal size and pyramidal vertex angles [96]. After texturing, the RCA (developed by Werner Kern in 1965 while working for the Radio Corporation of America.) cleaning procedure is a standard set of wafer cleaning steps to remove any organic and inorganic contaminants, which needs to be performed before the deposition of a-Si:H [97]. The first and second steps are performed with the alkali solution (NH_3•H_2O: H_2O_2: H_2O=1:1:5) and acid soluction (NH_3•H_2O: H_2O_2: H_2O=1: 1: 6) at 70–80°C for 10 minutes. An i-a-Si:H passivation layer and a p-type emitter are deposited on the front (illumination) side sequentially by PECVD. Afterward, on the rear of c-Si, an i-a-Si:H passivation layer and an n-type BSF layer are also prepared via the same method. Direct deposition of the doped layers on the surface of c-Si may result in poor interface properties as dopant incorporation would generate large recombination-active defects in amorphous silicon [98]. Besides, the passivation quality of i-a-Si:H may be deteriorated significantly when subsequent deposition of doped layers was not properly controlled [99]. Finally, TCO layers and metal electrodes are fabricated on the two sides of substrates. Contrary to the c-Si homojunction devices, TCO layers are necessary in SHJ cells [100] owing to poor lateral conductivity of the doped a-Si:H layers, and the front TCO layer also acts as an antireflection coating layer.

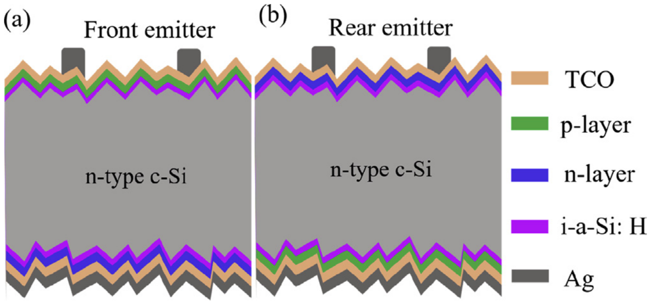

Fig. 6. Schematic drawings of the different SHJ cell structures: (a) front emitter and (b) rear emitter. SHJ, silicon heterojunction; c-Si, crystalline silicon; a-Si:H, hydrogenated amorphous silicon; TCO, transparent conductive oxide.

There is no doubt that the insertion of high-quality i-a-Si:H between c-Si and doped thin films is the key to obtain high performance of SHJ cells. An optimized i-a-Si:H film provides excellent chemical passivation mainly by saturating silicon dangling bonds, thus leading to a reduction in the interface defect density [101]. The optimized i-a-Si:H film is usually obtained close to the transition from amorphous to c-Si [102], but epitaxial growth has to be suppressed because of its detrimental effect on passivation [103,104]. Therefore, the experimental window for the high-quality i-a-Si:H film is narrow. For instance, Kim et al. [105] studied the effect of the hydrogen-to-silane dilution ratio on the passivation properties of the i-a-Si:H layers deposited on c-Si, and the quality of i-a-Si:H films was improved via a ratio of 2–4. In addition, Ge et al. [106] focused on optimizing i-a-Si:H films by varying substrate temperature, dilution ratio, and pressure independently, and the best passivation condition is obtained at a hydrogen-to-silane dilution ratio of 1 and a pressure of 66.7 Pa. Other groups reported an improved surface passivation of i-a-Si:H, followed by post–H-plasma treatment, which resulted from diffusion of hydrogen atoms to the heterointerface and subsequent dangling bond passivation [107–109].

2.2.2. Rear emitter

Watahiki et al. [110] achieved a rear emitter SHJ solar cell with the highest PCE of 23.43% (V_{oc} = 743 mV, FF = 80.7%, J_{SC} = 39.1 mA/cm^2) via introducing a seed layer between an n-type μc-Si layer and an i-a-Si:H layer. In addition to the aforementioned key passivation technology, Bivour et al. [111] also experimentally verified that the design of the RE cell lowered the restrictions on the lateral conductivity of the front side of TCO owing to an additional lateral transport path provided by the absorber and less demanding constraints on the design of the front side of the metal grid electrode.

Although there are less optical constraints for the p-type RE, more restricted optical and electrical constraints of the n-type window layer or front surface field need to be fulfilled simultaneously. Especially, the J_{sc} is limited by high light absorption of an n-type a-Si:H layer in the short wavelength range. Alloying with oxygen helps to reduce parasitic absorption further and, moreover, reduces reflection of the incoming light in case of SHJ cells [112]. Chen et al. [113] investigated the microstructures and properties of n-type a-Si:H window layers of SHJ solar cells via hydrogen dilution and found that an oxidation after treatment on the n-a-Si:H window layer is a potential choice for improving J_{sc} via apparently enhancing light absorption in c-Si at short wavelengths. Moreover, the results of the study by Zhang et al. [114] indicated that an n-type amorphous silicon oxide (a-SiO$_x$: H) film with the enlarged optical bandgap can also be applied to SHJ cells as a window n+ layer, to enhance the J_{sc}. For example, Mazzarella et al. [115,116] implemented n-type nc-SiO$_x$:H (two phase, silicon nanocrystals embedded into an a-SiO$_x$:H matrix) to enhance both transparency and conductivity and improved the *FF* of the SHJ devices.

The process of low-temperature preparation and eventually the high V_{oc}, resulting from the intrinsic a-Si:H passivation, make the SHJ cell one of the appropriate bottom cells. Not compatible with high-efficiency mesoscopic perovskite top cells, the SHJ cells have limited temperature tolerance owing to the low thermal stability of surface passivation by i-a-Si:H, restricting the subsequent processing temperatures to less than 250 °C, connected with planar low-temperature perovskites to constitute tandem cells.

3. Current status of monolithic 2T perovskite/silicon tandem cells

Despite the significant challenges in the monolithic perovskite/silicon tandem cells, such as process compatibility and current matching in the two subcells, the performance of monolithic perovskite/silicon tandem cells has been largely improved in the recent 4 years. The perovskite/homojunction cells are summarized in Fig. 7 and Table 2, and perovskite/heterojunction cells are illustrated in Fig. 8 and Table 3.

3.1. Perovskite/Si homojunction tandem cells

In 2015, Mailoa et al. [117] fabricated the first monolithic mesoscopic perovskite/standard full-area Al-BSF tandem cell with a stable PCE of 13.7% on 1 cm^2, and its structure and detailed performance parameter are shown in Fig. 7(a) and Table 2, respectively. In their work, a partially crystalline n^{++}-a-Si (deposited by PECVD)/p^{++}-c-Si (the emitter of the bottom cell) tunneling junction facilitated carrier recombination, with Ag nanowires as the top transparent electrode. The external quantum efficiency (EQE) of the semitransparent perovskite cell integrated to 17.3 mA/cm^2 illuminated through the TiO$_2$ layer, but the EQE only integrated to 11.4 mA/cm^2 illuminated through the spiro-OMeTAD layer owing to its parasitic absorption. There are no front texturing and passivation for the silicon bottom cells.

As shown in Fig. 7(b), in the research by Werner et al, the SiO$_2$ passivation layer on the rear side was opened by laser patterning, and phosphorus was implanted for local contact and BSF formation [118]. Through investigating the thickness effect of a high-temperature-stable zinc tin oxide (ZTO) recombination layer on the optical interference pattern in the device, with molybdenum oxide (MoO$_x$)/indium tin oxide (ITO)/hydrogenated indium oxide as the top transparent electrode, a monolithic mesoscopic perovskite/PERL tandem cell with up to 16% efficiency on 1.43 cm^2 was successfully achieved finally. Obviously, as indicated in Table 2, compared with the first perovskite/standard full-area Al-BSF tandem cell, the V_{oc} of the perovskite/PERL tandem cell was improved by ~100 mV, which mainly resulted from a boost of the silicon bottom cell with a rear passivation layer. However, the performance of the perovskite/PERL tandem cell was limited by a low *FF* of 64.8% owing to high series resistance. Furthermore, in Fig. 7(c), Wu et al. [119] demonstrated that the silicon bottom cell with passivated front and rear surfaces maintained a high V_{oc}, while an array of Cr/Pd/Ag metal stacks was applied for the contact openings between the ITO recombination layer and the boron-doped emitter to minimize the contact resistance and obtain a relatively good *FF* (>0.75). To enhance the light-trapping capability, the rear-textured c-Si was coated with low refractive index SiN$_x$ to enhance infrared reflection, and they successfully developed a monolithic mesoscopic perovskite/PERT tandem cell with a PCE of 22.5% (steady state) on 1 cm^2. Recently, Zheng et al. [120] showed the first monolithic planar perovskite/PERT tandem cell without the additional step of fabricating an interface layer for electrical connection between the two subcells, yielding a steady-state efficiency of 20.5% on 4 cm^2 and 17.1% on 16 cm^2. In their work, solution-processed SnO$_2$ has been effective in providing dual functions in the monolithic tandem, serving as an electron transport layer for the perovskite cell and as a recombination layer. Moreover, in their further research, as presented in Fig. 7(d), with a new metal grid design, a mixed perovskite absorber, and a rear-textured surface, a steady-state 21.8% efficiency was achieved on 16 cm^2 [121].

3.2. Perovskite/SHJ tandem cells

To be compatible with the currently best-performing SHJ technology, the high-temperature mesoporous or compact TiO$_2$ layer should be changed or replaced by another electron selection layer processed at low temperatures. As expected, Albrecht et al. [122] proposed a new approach for low-temperature (below 120 °C) processing of the semitransparent perovskite subcell via electron-selective contact SnO$_2$ prepared by ALD and successfully demonstrated the first monolithic planar low-temperature processed perovskite/planar SHJ with FE tandem cell with a stabilized PCE of 18.1% on 0.16 cm^2, as shown in Fig. 8 (a). Then, Werner et al. [123] implemented sputtered indium zinc oxide (IZO) as a recombination layer, polyethylenimine/phenyl-C$_{61}$-butyric acid methyl ester bilayer as an electron transport layer, and achieved a tandem cell with a PCE of 21.2% and 19.2% for cell areas of 0.17 cm^2 and 1.22 cm^2, respectively, when measured at maximum power point tracking during several minutes. And they also presented the effects of thicknesses for IZO and spiro-OMeTAD layers on tandem cell photocurrent generation. In addition, Fan et al. [124] varied the bandgap of the perovskite absorber ranging from ~1.55 to 1.69 eV via solution process to achieve better current matching between the two subcells. Zhu et al. [125] modified light utilization and conductivity through adjusting the thickness of the buffer layer and sputtering power of the transparent electrode and applied solvent engineering to balance light absorbance and transmittance of perovskite films in tandem devices, successfully obtaining an optimal efficiency of 22.8% on 0.13 cm^2 [126]. Besides the aforementioned optimization on the top cell, the results of the study by Ren et al [127] indicated that the near-infrared wavelength response in the planar SHJ bottom cell was increased when a wide bandgap and low-refractive-index nc-SiO$_x$:H layer was used for BSF. Besides the parasitic absorption of spiro-OMeTAD layers, it should be noted that poor light trapping is another important issue owing to application of double-side polished silicon wafers, limiting the experimental J_{sc} below 19 mA/cm^2.

First of all, while keeping the front side flat to remain compatible with solution-processed top cells, a rear random pyramid

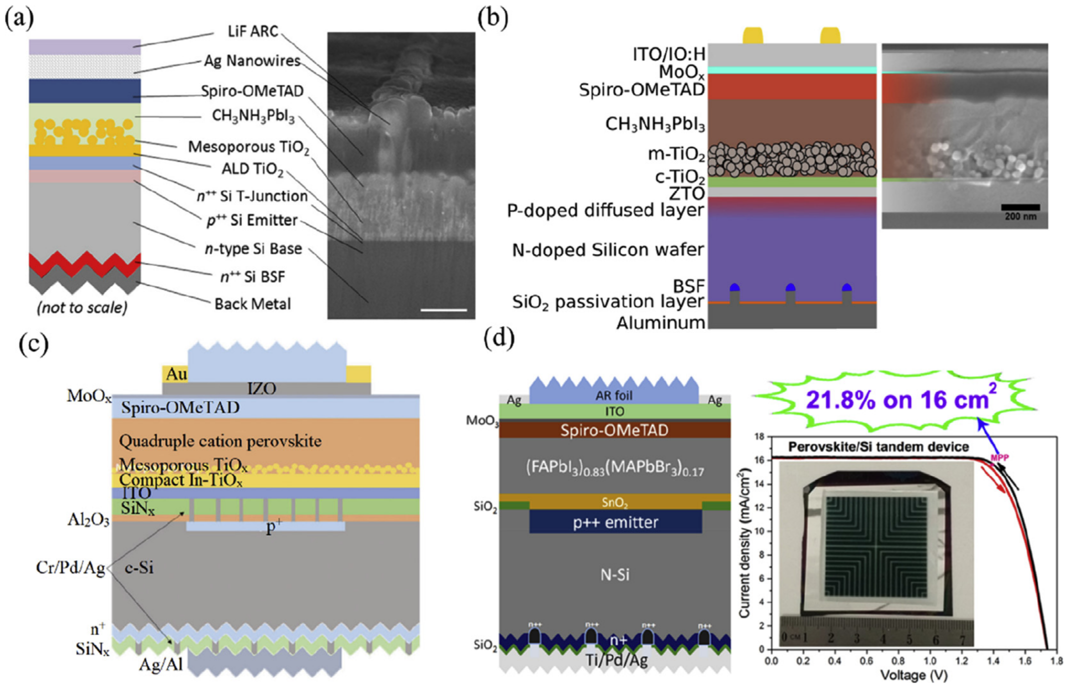

Fig. 7. The progress of perovskite/silicon homojunction tandem cells: (a) the first monolithic mesoscopic perovskite/standard full-area Al-BSF tandem cell, and the polished scanning electron microscope (SEM) image is taken at 45° tilt to show the Ag nanowire mesh (500-nm scale bar) [117], (b) the monolithic mesoscopic perovskite/PERL tandem cell, and the SEM image shows a cross section of a typical perovskite top cell, (m-TiO_2 = scaffold layer; c-TiO_2 = compact electron transport layer; and spiro-OMeTAD = hole transport layer.) [118], (c) the monolithic mesoscopic perovskite/PERT tandem cell [119], and (d) the monolithic planar perovskite/PERT tandem cell without an additional recombination layer [121]. ARC, anti-reflection layer; Al-BSF, aluminum back surface field; PERL, passivated emitter and rear locally diffused; PERT, passivated emitter and rear totally diffused; ALD, atomic layer deposition; ITO, indium tin oxide; ZTO, zinc tin oxide.

Table 2
Summaries of 2T perovskite/c-Si homojunction tandem cells.

Bottom cell	Substrates	Recombination layer	V_{oc} (V)	J_{sc} (mA/cm^2)	FF (%)	PCE (%)	Steady-state or certified PCE (%)	Area (cm^2)	Year
Al-BSF	Rear-texturing	n^{++}/p^{++}	1.58	11.5	75.0	–	13.7	1.00	2015 [117]
PERL	Planar	ZTO	1.64	15.3	64.8	16.3	16.0	1.43	2016 [118]
PERT	Rear-texturing	ITO	1.75	17.6	73.8	22.8	22.5	1.00	2017 [119]
PERT	Planar	w/o	1.68	16.1	78.0	21.0	20.5	4.00	2018 [120]
PERT	Planar	w/o	1.66	15.6	68.0	17.6	17.1	16.00	
PERT	Rear-texturing	w/o	1.74	16.2	78.0	21.9	21.8	16.00	2018 [121]

FF, fill factor; PCE, power conversion efficiency; Al-BSF, aluminum back surface field; PERL, passivated emitter and rear locally diffused; ZTO, zinc tin oxide; PERT, passivated emitter and rear totally diffused; ITO, indium tin oxide; w/o, without; –, not reported.

texture of the bottom cell could be implemented to enhance light trapping effectively. Compared with their previous report, Werner et al. [123] introduced a rear-textured SHJ bottom cell to enhance the EQE spectra in the near-infrared region, improving the current density of the bottom cell by 0.77 mA/cm^2, which resulted in a steady-state efficiency of 20.5% for an aperture area of 1.43 cm^2 [128]. Second, avoiding window layers with high parasitic absorption such spiro-OMeTAD is a better choice to achieve higher current densities and efficiencies in monolithic tandems by adopting an inverted p-i-n perovskite configuration. As shown in Fig. 8(b), with a stack silicon nanoparticle/silver as the rear reflector, a bilayer of SnO_2 and ZTO as the window layer with minimal parasitic absorption, Bush et al. realized a 23.6% efficient p-i-n perovskite/rear texturing SHJ with RE tandem cell with improved stability [129]. It is the first time that a p-i-n structure tandem with a high J_{sc} of 18.1 mA/cm^2 is achieved, but the V_{oc} is only 1.65 V. Therefore, further efforts can be made to improve the performance of tandem cells. Furthermore, with a similar configuration, Chen et al. [130] demonstrated that grain engineering was successfully applied for the achievement of perovskite/silicon tandem cells with a PCE more than 25.4% through combined MACl and MAH_2PO_2 additives in perovskite precursors.

So far, TCO as an intermediate recombination layer has been used for the current design of perovskite/Si tandems. However, high lateral conductivity of TCO promotes shunt paths through the top cell. For this reason, a hydrogenated nanocrystalline silicon (nc-Si:H) recombination layer was used, providing sufficient vertical conductivity while exhibiting low lateral conductivity. As expected, the low lateral conductivity of the nc-Si:H recombination layer with a highly anisotropic conductivity enabled a 12.96 cm^2 tandem cell with a steady-state efficiency of 18% through mitigating shunt paths, laying the foundation for high-efficiency large-area perovskite/silicon tandem solar cells [131]. In addition, the reflection and parasitic absorption losses can be decreased effectively by the nc-Si:H recombination junction, in comparison with a commonly used TCO recombination layer. In detail, the bottom cell photocurrent was increased (>1 mA/cm^2) by the application of the p-nc-Si:H/n-nc-Si:H junction for the n-i-p perovskite/rear-textured SHJ

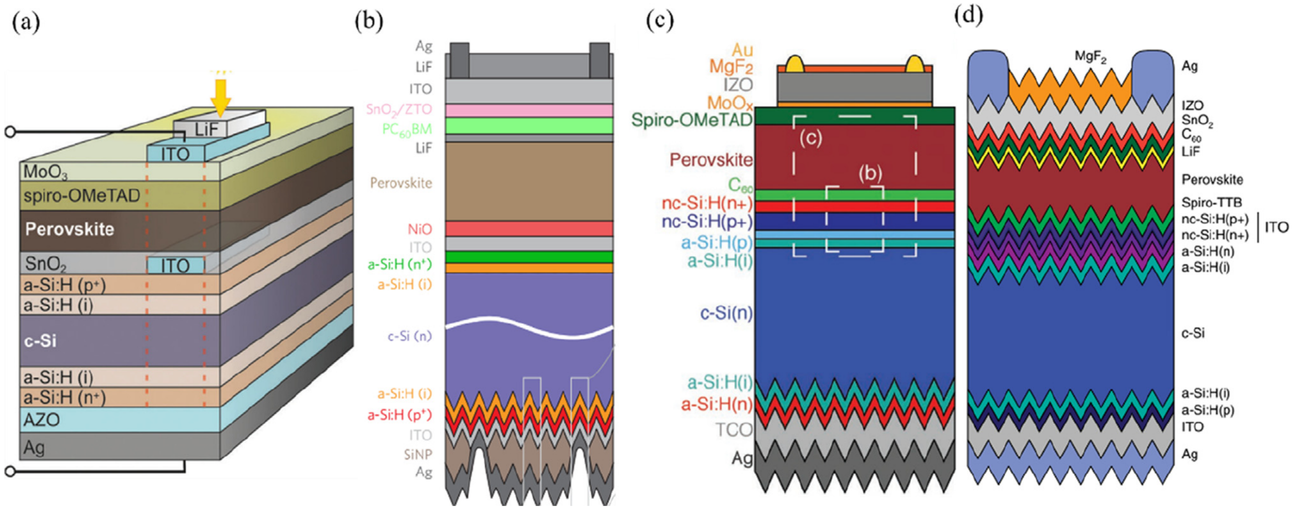

Fig. 8. The typically structural evolution of perovskite/SHJ tandem cells: (a) the first monolithic n-i-p planar perovskite/planar SHJ with FE tandem cell [122], (b) p-i-n perovskite/rear texturing SHJ with RE tandem cell [129], (c) n-i-p perovskite/rear texturing SHJ with FE tandem cell [131], and (d) p-i-n perovskite/double-side texturing SHJ with RE tandem cell [134]. AZO, aluminum doped zinc oxide; SHJ, silicon heterojunction; FE, front emitter; RE, rear emitter; a-Si:H, hydrogenated amorphous silicon; ITO, indium tin oxide; SiNP, silicon nanoparticle; TCO, transparent conductive oxide; IZO, indium zinc oxide.

Table 3
Summaries of 2T perovskite/SHJ tandem cells.

Bottom cell	Substrates	Recombination layer	V_{oc} (mV)	J_{sc} (mA/cm^2)	*FF* (%)	PCE (%)	Steady-state or certified PCE (%)	Area (cm^2)	Year
FE	Planar	ITO	1.79	14.0	79.5	19.9	18.1	0.16	2015 [122]
			1.69	15.8	79.9	21.4	21.2	0.17	2015 [123]
FE	Planar	IZO	1.70	16.1	70.9	19.5	19.2	1.22	
FE	Planar	ITO	1.73	15.3	79	20.6	18	0.03	2017 [124]
FE	Planar	ITO	1.78	17.82	75	22.8	–	0.13	2017 [126]
FE	Rear-texturing	IZO	1.72	16.4	73.1	20.6	20.5	1.43	2016 [128]
RE	Rear-texturing	ITO	1.65	18.1	79.0	23.6	23.6[a]	1.00	2017 [129]
FE	Rear-texturing	p-nc-Si: H/n-nc-Si:H	1.75	16.8	77.5	22.8	22.0	0.25	2017 [131]
			1.78	16.5	74.4	21.8	21.2	1.43	
			1.77	16.5	65.4	19.1	18.0	12.96	
RE	Rear-texturing	n-nc-SiO$_x$+ITO	1.79	19.02	74.6	25.4	25.2[a]	1.00	2019 [132]
RE	Double-side texturing	n-nc-Si:H/p-nc-Si:H	1.79	19.5	73.1	25.5	25.2[a]	1.419	2018 [135]
RE	Rear-texturing	ITO	1.77	18.4	77	25	–	1	2018 [136]
RE	Rear-texturing	ITO	1.76	18.5	78.5	25.5	–	0.77	2018 [137]
RE	Rear-texturing	ITO	1.76	19.22	76.5	26.0	25.0[a]	1	[138]
–	–	–	–	–	–	–	28[a]	1	2018 [23]

–, not reported; 2T, two-terminal; SHJ, silicon heterojunction; *FF*, fill factor; PCE, power conversion efficiency; FE, front emitter; ITO, indium tin oxide; IZO, indium zinc oxide; RE, rear emitter; nc-Si:H, hydrogenated nanocrystalline silicon,

[a] Certified efficiencies.

with FE tandem cell in Fig. 8(c). Furthermore, Mazzarella et al. [132] proposed the use of nc-SiO$_x$:H as the interlayer between the silicon and perovskite subcells, which reduced the infrared reflection losses in the tandem cells processed on a flat silicon substrate and finally resulted in a 1.4 mA/cm^2 current gain in the silicon bottom cell.

Unfortunately, to be compatible with the solution-based spin-coating perovskite absorber, the J_{sc} of the tandem cell was limited owing to the lack of light trapping normally provided by the front random pyramid texture of the silicon wafer. The simulation results further indicated that a high-efficiency tandem device with the double-side texturing Si substrate was an ideal configuration [133,134]. As expected, based on their previous research about improved optics in perovskite/silicon tandem cells with a nc-Si:H recombination junction, Sahli et al. [135] developed the p-i-n perovskite/double-side texturing SHJ with RE tandem cell with a current density of 19.5 mA/cm^2 and a certified steady-state PCE of 25.2% through a hybrid two-step deposition method combining sequential coevaporation with spin coating to yield conformal perovskite absorber layers on the micrometer-sized pyramids of textured SHJ bottom cells in Fig. 8(d). Based on the p-i-n perovskite/rear-textured SHJ with RE tandem cell, Bush et al. [136] continued to minimize current and voltage losses to reach 25% efficient perovskite/silicon tandem cells. In their work, optical optimizations were realized mainly via thinning out the top transparent electrode and introducing a polydimethylsiloxane (PDMS) stamp reflection layer with random, pyramidal texture. Guided by the same concept, a textured light management (TLM) foil on the front-side of p-i-n perovskite/rear-textured SHJ with RE tandem cell was used by Jost et al. [137], and the PCE was significantly improved from 23.4% to 25.5%. As illustrated in Table 3, although the J_{sc} of rear-textured tandem cells with the addition of TLM such as PDMS or foils is still lower than that of fully textured perovskite/silicon tandem cells, the former may be another good choice to obtain high-efficiency tandem cells owing to the simple deposition of perovskite layers with spin coating. Currently, Oxford PV reported a perovskite/silicon tandem with a world record PCE of 28% certified by the National Renewable

Energy Laboratory [23], but there is no detailed information about their device structure.

4. Conclusion and perspectives

Looking back to the development history of perovskite/c-Si homojunction tandem cells in recent years, the PCE of mesoscopic perovskite/c-Si homojunction tandem cells was improved quickly from 13.7% to 22.5% on 1 cm^2. Moreover, the achievement of the monolithic low-temperature planar perovskite/PERT tandem cell with a steady-state efficiency of 21.8% on 16 cm^2 paves a way for their large-area scale-up. However, in the current design of the bottom cell, although the passivation techniques have been applied, the used PERX bottom cell with a V_{oc} of ~620 mV is far from that for an optimized homojunction design. The structural evolution of perovskite/SHJ tandem cells and their progress of performance improvement indicate that a SHJ bottom cell with a high V_{oc} up to 750 mV is an appropriate c-Si bottom cell, which has been used adequately. However, the SHJ bottom cell applied in the tandem cells is far below the corresponding parameter of the single-junction SHJ with high performance. Therefore, there is still a large room for improving tandem solar cells based on SHJ bottom cells.

A huge progress has been achieved for mesoporous n-i-p, regular planar n-i-p devices, and inverted planar p-i-n PSCs. For the mesoporous structure, mesoporous TiO_x is typically inserted between the compact TiO_x and perovskite layer to form the interconnected nanoparticle network, enhancing the flux of electrons toward the TCO electrode from the photoabsorber, which benefits for a high J_{sc} [139,140]. The hysteresis of the planar n-i-p configuration makes it difficult to obtain a reliable PCE owing to charge accumulation induced by ion migration in the perovskite layer [141,142]. It is clear that the inverted planar p-i-n perovskite cells can now yield high efficiency and negligible *J-V* hysteresis with fullerene as the electron transport layer and slot-die coating and roll-to-roll techniques used to produce large-area and flexible devices. However, the band alignment between perovskite and the hole transport layer leads to an imperfect ohmic contact and a consequent V_{oc} loss in the inverted planar p-i-n perovskite structure [143,144]. Taking into consideration the advantages and disadvantages of the aforementioned three structures, the planar perovskite top cell is the main consideration in our following prediction.

On the basis of previous theoretical work and the state-of-the art experimental results, we carried out a semiempirical analysis for the possible and realistic PCE of perovskite/Si tandem cells under Air Mass 1.5 Global. The performance of single-junction perovskite and c-Si cells can provide an efficient reference to evaluate the performance of tandem cells, so the performance parameters of single-champion junction cells are summarized in Table 4. To pair a Si bottom cell in a monolithic tandem approach, the optimum bandgap for the top cell material is $E_g \approx 1.6-1.7$ eV [147]. Therefore, as shown in Table 4, the best-performing perovskite top cells with a wide bandgap at low temperature were used in our deduction. In our analysis, the PCE ($V_{oc} \times J_{sc} \times FF/P_{in}$, where P_{in} is the power density of the incident light) is obtained through the following approaches: (i) the J_{sc} is assumed to be half of the J_{sc} of the world record c-Si cell in the entire absorption range when the current match is well adjusted between the subcells [148], (ii) the V_{oc} is the sum of the subcells, and the V_{oc} of the subcells in the tandem stack is estimated by the logarithmic dependence of V_{oc} on the photocurrent density [149,150]; a V_{oc} loss of about 15 mV for the single-junction c-Si cells with the J_{sc} reducing from 40 to 21 mA/cm^2, a negligible V_{oc} loss for the perovskite devices with a slight reduction of J_{sc}, a V_{oc} loss of about 20 mV mainly due to the electrical loss at the tunneling recombination layer [151], (iii) the *FF* is assumed to be the state-of-the art value of the corresponding bottom c-Si [152,153]. Based on these considerations, the predicted achievable PCEs of perovskite/Si tandem cells with different device designs are deduced in Table 5. Current studies about the application of c-Si homojunction bottom cells have been focused on traditional c-Si cells with full-area Al-BSF or PERX cells, and there is no report about the c-Si homojunction cell with a TOPCon structure as bottom cells. In our opinion, a TOPCon cell without local contact openings is another good choice to be an appropriate candidate of the c-Si homojunction bottom cell, which also presents an excellent passivation quality through a stack of an ultrathin tunnel oxide layer and a heavily doped poly-Si layer. The PCE of planar n-i-p perovskite/n-TOPCon is expected to reach about 33.8% in the future ($V_{oc} = 1.91$ V, $FF = 83.3\%$, $J_{sc} = 21.25$ mA/cm^2). It should be noted that p-type PERC devices are one of the dominant solar cell structures in the PV market today associated with p-type c-Si wafers, so the advanced industrial technology of the *p*-PERC device provides a convenient condition to realize its mass production.

Generally, the PERC devices as bottom cells are the favorable choice for the current development of industry owing to compatibility with the production line. On the other hand, TOPCon and SHJ, both of which demand special requirements on passivation quality, acting as bottom cells, are the main options for researchers to obtain devices with high performance. Especially, TOPCon, with the establishment of mature production line, could be another appropriate bottom cell for large-scale production.

In summary, no matter what kind of c-Si cells (traditional c-Si with full-area Al-BSF, PERX, TOPCon, and SHJ) are selected, they can be appropriate candidates of the c-Si bottom cell for monolithic perovskite/silicon tandem solar cells owing to their specific advantages, and further optimized passivation design of the c-Si bottom cell should be paid enough attention. The PCEs of corresponding tandem cells are expected to exceed 30%, which is about a 5% increase compared with the single-junction cell with a PCE of 25%. Although there are still many challenges in the development of tandem cells, such as reliability and upscaling, rapid progress is being made. We believe the monolithic 2T perovskite/Si tandem cells with a PCE more than 30% will be achievable.

Table 4

Performance parameters of single-junction champion devices in our analysis.

The detailed subcell structure	V_{oc} (V)	J_{sc} (mA/cm^2)	*FF* (%)	PCE (%)	Steady-state or certified PCE (%)
p-PERC	0.696	40.3	81.4	22.8 [51]	/
n-TOPCon	0.725	42.5	83.3	25.7 [84]	/
SHJ	0.738	40.8	83.5	25.1 [95]	/
Planar n-i-p $Cs_{0.05}MA_{0.15}FA_{0.8}Pb(I_{0.75}Br_{0.25})_3$, $E_g = 1.65$ eV	1.22	21.2	80.5	20.8	20.7 [145]
Planar p-i-n $(FA_{0.95}PbI_{2.95})_{0.85}(MAPbBr_3)_{0.15}$, $E_g = 1.62$ eV	1.175	21.86	81.37	21.51	20.91 [146]

FF, fill factor; PCE, power conversion efficiency; PERC, passivated emitter and rear cell; TOPCon, tunnel oxide passivated contact; SHJ, silicon heterojunction.

Table 5
The predicted achievable PCEs of perovskite/silicon tandem cells.

The bottom cell structure	The detailed tandem structure	V_{oc} (V)	J_{sc} (mA/cm^2)	*FF* (%)	PCE (%)
Homojunction	Planar p-i-n perovskite/p-PERC	1.836	20.15	81.4	30.1
	Planar n-i-p perovskite/n-TOPCon	1.91	21.25	83.3	33.8
Heterojunction	Planar n-i-p perovskite/SHJ	1.923	20.4	83.5	32.8

FF, fill factor; PCE, power conversion efficiency; PERC, passivated emitter and rear cell; TOPCon, tunnel oxide passivated contact; SHJ, silicon heterojunction.

Conflict of interests

The authors declare that they have no known competing financial interests or personal relationships that could have appeared to influence the work reported in this article.

Acknowledgments

The authors gratefully acknowledge the supports from National Key Research and Development Program of China (Grant no. 2018YFB1500103), the National Natural Science Foundation of China (Grant no. 61674084), the Overseas Expertise Introduction Project for Discipline Innovation of Higher Education of China (Grant no. B16027), Tianjin Science and Technology Project (grant no. 18ZXJMTG00220), and the Fundamental Research Funds for the Central Universities, Nankai University (Grant nos. 63191736, ZB19500204).

References

[1] N. Kannan, D. Vakeesan, Solar energy for future world: a review, Renew. Sustain. Energy Rev. 62 (2016) 1092–1105.

[2] M.A. Green, Solar Cells: Operating Principles, Technology, and System Applications, Prentice-Hall, Inc., Englewood Cliffs, NJ, 1982.

[3] M.A. Green, Commercial progress and challenges for photovoltaics, Nat. Energy 1 (2016) 15015.

[4] C. Battaglia, A. Cuevas, S. De Wolf, High-efficiency crystalline silicon solar cells: status and perspectives, Energy Environ. Sci. 9 (2016) 1552–1576.

[5] A.D. Vos, Detailed balance limit of the efficiency of tandem solar cells, J. Phys. D Appl. Phys. 13 (2000) 839.

[6] J.Y. Kim, K. Lee, N.E. Coates, D. Moses, T.Q. Nguyen, M. Dante, A.J. Heeger, Efficient tandem polymer solar cells fabricated by all-solution processing, Science 317 (2007) 222–225.

[7] J. Kim, Z.R. Hong, G. Li, T.B. Song, J. Chey, Y.S. Lee, J.B. You, C.C. Chen, D.K. Sadana, Y. Yang, 10.5% efficient polymer and amorphous silicon hybrid tandem photovoltaic cell, Nat. Commun. 6 (2015) 6391.

[8] B.F. Liu, L.S. Bai, T.T. Li, C.C. Wei, B.Z. Li, Q. Huang, D.K. Zhang, G.C. Wang, Y. Zhao, X.D. Zhang, High efficiency and high open-circuit voltage quadruple-junction silicon thin film solar cells for future electronic applications, Energy Environ. Sci. 10 (2017) 1134–1141.

[9] M. Fischer, H. Tan, J. Melskens, R. Vasudevan, Miro Zeman, Arno H.M. Smets, High pressure processing of hydrogenated amorphous silicon solar cells: relation between nanostructure and high open-circuit voltage, Appl. Phys. Lett. 106 (2015), 043905.

[10] D.L. Staebler, C.R. Wronski, Reversible conductivity changes in discharge-produced amorphous Si, Appl. Phys. Lett. 31 (1977) 292–294.

[11] M. Stutzmann, J. Nunnenkamp, M.S. Brandt, A. Asano, Fast metastable defect-creation in amorphous silicon by femtosecond light pulses, Phys. Rev. Lett. 67 (1991) 2347–2350.

[12] H. Plagwitz, B. Terheiden, R. Brendel, Staebler-Wronski-like formation of defects at the amorphous-silicon-crystalline silicon interface during illumination, J. Appl. Phys. 103 (2008) 1246.

[13] M.A. Green, Y. Hishikawa, E.D. Dunlop, D.H. Levi, J. Ho-Baillie, A.W.Y. Hohl-Ebinger, Solar cell efficiency tables (version 52), Prog. Photovolt. Res. Appl. 26 (2018) 427–436.

[14] K. Sasaki, T. Agui, K. Nakaido, N. Takahashi, R. Onitsuka, T. Takamoto, in: 9th International Conference on Concentrating Photovoltaics Systems, Miyazaki, Japan, 2013, pp. 22–26.

[15] W. Choi, C.Z. Kim, C.S. Kim, W. Heo, T. Joo, S.Y. Ryu, H. Kim, H. Kim, H.K. Kang, S. Jo, A repeatable epitaxial lift-off process from a single GaAs substrate for low-cost and high-efficiency III-V solar cells, Adv. Energ. Mater. 4 (16) (2014).

[16] J. Schermer, G.J. Bauhuis, P. Mulder, W.J. Meulemeesters, E. Haverkamp, M.M.A.J. Voncken, High rate epitaxial lift-off of InGaP films from GaAs substrates, Appl. Phys. Lett. 76 (2000) 2131–2133.

[17] H. Yoon, J.E. Granata, P. Hebert, R.R. King, C.M. Fetzer, P.C. Colter, K.M. Edmondson, D. Law, G.S. Kinsey, D.D. Krut, J.H. Ermer, M.S. Gillanders, N.H. Karam, Recent advances in high-efficiency III-V multi-junction solar cells for space applications: ultra triple junction qualification, Prog. Photovolt. Res. Appl. 13 (2016) 133–139.

[18] H. Cotal, C. Fetzer, J. Boisvert, G. Kinsey, R. King, P. Hebert, H. Yoon, N. Karam III, V multijunction solar cells for concentrating photovoltaics, Energy Environ. Sci. 2 (2009) 174–192.

[19] Y. Nakao, Silicon-based cross-coupling reaction: an environmentally benign version, Chem. Soc. Rev. 40 (2011) 4893.

[20] D.M. Chapin, C.S. Fuller, G.L. Pearson, A new silicon p-n junction photocell for converting solar radiation into electrical power, J. Appl. Phys. 25 (1954) 676–677.

[21] K. Yoshikawa, W. Yoshida, T. Irie, H. Kawasaki, K. Konishi, H. Ishibashi, T. Asatani, D. Adachi, M. Kanematsu, H. Uzu, K. Yamamoto, Exceeding conversion efficiency of 26% by heterojunction interdigitated back contact solar cell with thin film Si technology, Sol. Energy Mater. Sol. Cells 173 (2017) 37–42.

[22] A. Richter, M. Hermle, S. Glunz, Crystalline silicon solar cells reassessment of the limiting efficiency for crystalline silicon solar cells, IEEE J. Photovolt. 3 (2013) 1184–1191.

[23] NREL Best Research-Cell Efficiencies. https://www.nrel.gov/pv/cell-efficiency.html.

[24] S. De Wolf, J. Holovsky, S.J. Moon, P. Loper, B. Niesen, M. Ledinsky, F.J. Haug, J.H. Yum, C. Ballif, Organometallic halide perovskites: sharp optical absorption edge and its relation to photovoltaic performance, J. Phys. Chem. Lett. 5 (2014) 1035–1039.

[25] S.D. Stranks, G.E. Eperon, G. Grancini, C. Menelaou, M.J.P. Alcocer, T. Leijtens, L.M. Herz, A. Petrozza, H.J. Snaith, Electron-hole diffusion lengths exceeding 1 micrometer in an organometal trihalide perovskite absorber, Science 342 (2013) 341–344.

[26] G.E. Eperon, Formamidinium lead trihalide: a broadly tunable perovskite for efficient planar heterojunction solar cells, Energy Environ. Sci. 7 (2014) 982–988.

[27] T. Leijtens, K.A. Bush, P. Rohit, R. Prasanna, M.D. McGehee, Opportunities and challenges for tandem solar cells using metal halide perovskite semiconductors, Nat. Energ. 3 (2018) 828–838.

[28] N. Torabi, A. Behjat, Y.H. Zhou, P. Docampo, R.J. Stoddard, H.W. Hillhouse, T. Ameri, Progress and challenges in perovskite photovoltaics from single- to multi-junction cells, Mater, Today Energ 12 (2019) 70–94.

[29] Z.W. Qiu, Z.Q. Xu, N.X. Li, N. Zhou, Y.H. Chen, X.X. Wan, J.L. Liu, N. Li, X.T. Hao, P.Q. Bi, Q. Chen, B.Q. Cao, H.P. Zhou, Monolithic perovskite/Si tandem solar cells exceeding 22% efficiency via optimizing top cell absorber, Nano Energy 53 (2018) 798–807.

[30] Y. Jiang, I. Almansouri, S. Huang, T. Young, Y. Li, Y. Peng, Q.C. Hou, L. Spiccia, U. Bach, Y.B. Cheng, M.A. Green, A. Ho-Baillie, Optical analysis of perovskite/silicon tandem solar cells, J. Mater. Chem. C 4 (2016) 5679–5689.

[31] A. Luque, S. Hegedus, Handbook of Photovoltaic Science and Engineering, Wiley, Chichester, UK, 2003.

[32] C.D. Bailie, M.G. Christoforo, J.P. Mailoa, A.R. Bowring, E.L. Unger, W.H. Nguyen, J. Burschka, N. Pellet, J.Z. Lee, M. Gratzel, R. Noufi, T. Buonassisi, A. Salleo, M.D. McGehee, Semi-transparent perovskite solar cells for tandems with silicon and CIGS, Energy Environ. Sci. 8 (2015) 956–963.

[33] M. Jaysankar, W. Qiu, M.V. Eerden, T. Aernouts, R. Gehlhaar, M. Debucquoy, U.W. Paetzold, J. Poortmans, Four-terminal perovskite/silicon multijunction solar modules, Adv. Energ. Mater. 7 (2017) 1602807.

[34] M. Jaysankar, M. Filipic, B. Zielinski, R. Schmager, W.Y. Song, W.M. Qiu, U.W. Paetzold, T. Aernouts, M. Debucquoy, R. Gehlhaar, J. Poortmans, Perovskite-silicon tandem solar modules with optimised light harvesting, Energy Environ. Sci. 11 (2018) 1489.

[35] H. Kanda, A. Uzum, A.K. Baranwal, T.A.N. Peiris, T. Umeyama, H. Imahori, H. Segawa, T. Miyasaka, S. Ito, Analysis of sputtering damage on I-V curves for perovskite solar cells and simulation with reversed diode model, J. Phys. Chem. C 120 (2016) 28441–28447.

[36] J. Werner, G. Dubuis, A. Walter, P. Loper, S.J. Moon, S. Nicolay, M. Morales-Masis, S. De Wolf, B. Niesen, C. Ballif, Sputtered rear electrode with broadband transparency for perovskite solar cells, Sol. Energy Mater. Sol. Cells 141 (2015) 407–413.

[37] J. Meyer, S. Hamwi, M. Kroger, W. Kowalsky, T. Riedl, A. Kahn, Transition metal oxides for organic electronics: energetics, device physics and applications, Adv. Mater. 24 (2012) 5408–5427.

[38] H. Uzu, M. Ichikawa, M. Hino, K. Nakano, T. Meguro, J.L. Hernandez, H.S. Kim, N.G. Park, K. Yamamoto, High efficiency solar cells combining a perovskite and a silicon heterojunction solar cells via an optical splitting system, Appl. Phys. Lett. 106 (2015) 1433–1435.

[39] Y. Li, H.W. Hu, B.B. Chen, T. Salim, J. Zhang, J.N. Ding, N.Y. Yuan, Y.M. Lam, Reflective perovskite solar cells for efficient tandem application, J. Mater. Chem. C 5 (2016) 134−139.

[40] F.H. Hou, C. Han, O. Isabella, L.L. Yan, B. Shi, J.F. Chen, S.C. An, Z.X. Zhou, W. Huang, H.Z. Ren, Q. Huang, G.F. Hou, X.L. Chen, Y.L. Li, Y. Ding, G.C. Wang, C.C. Wei, D.K. Zhang, M. Zeman, Y. Zhao, X.D. Zhang, Inverted pyramidally-textured PDMS antireflective foils for perovskite/silicon tandem solar cells with flat top cell, Nano Energy 56 (2019) 234−240.

[41] T. Todorov, T. Gershon, O. Gunawan, Y.S. Lee, C. Sturdevant, L.Y. Chang, S. Guha, Monolithic perovskite-CIGS tandem solar cells via in situ band gap engineering, Adv. Energ. Mater. 5 (2016).

[42] K. Jager, L. Korte, B. Rech, S. Albrecht, Numerical optical optimization of monolithic planar perovskite-silicon tandem solar cells with regular and inverted device architectures, Opt. Express 25 (2017) A473.

[43] H. Kanda, N. Shibayama, A. Uzum, T. Umeyama, H. Imahori, K. Ibi, S. Ito, Effect of silicon surface for perovskite/silicon tandem solar cells: flat or textured ? ACS Appl. Mater. Interfaces 10 (2018) 35016−35024.

[44] M.A. Melehy, On the theory of homojunction and heterojunction solar cells, Int. J. Electron. 44 (1987) 211−217.

[45] A. Descoeudres, Z.C. Holman, L. Barraud, S. Morel, S. De Wolf, C. Ballif, 21% Efficient silicon heterojunction solar cells on n- and p-type wafers compared, IEEE J. Photovolt. 3 (2013) 83−89.

[46] M. Mews, M. Liebhaber, B. Rech, L. Korte, Valence band alignment and hole transport in amorphous/crystalline silicon heterojunction solar cells, Appl. Phys. Lett. 107 (2015), 013902.

[47] H. Mimura, Y. Hatanaka, Carrier transport mechanisms of p-type amorphous−n-type crystalline silicon heterojunctions, J. Appl. Phys. 71 (1992) 2315−2320.

[48] T.F. Schulze, L. Korte, E. Conrad, M. Schmidt, B. Rech, Electrical transport mechanisms in a-Si: H/c-Si heterojunction solar cells, J. Appl. Phys. 107 (2010) 3518−3894.

[49] C.H. Lin, S.Y. Tsai, S.P. Hsu, M.H. Hsieh, Structural properties of the solidified-Al/regrown-Si structures of printed Al contacts on crystalline Si solar cells, Sol. Energy Mater. Sol. Cells 92 (2008) 986−991.

[50] Y. Gassenbauer, K. Ramspeck, B. Bethmann, K. Dressler, J.D. Moschner, M. Fiedler, E. Brouwer, R. Drossler, N. Lenck, F. Heyer, M. Feldhaus, A. Seidl, M. Muller, A. Metz, Rear-surface passivation technology for crystalline silicon solar cells: a versatile process for mass production, IEEE J. Photovolt. 3 (2012) 125−130.

[51] A.W. Blakers, A.H. Wang, A.M. Milne, J.H. Zhao, M.A. Green, 22.8% efficient silicon solar cell, Appl. Phys. Lett. 55 (1989) 1363−1365.

[52] M.A. Green, A.W. Blakers, J.Q. Shi, E.M. Keller, S.R. Wenham, 19.1% efficient silicon solar cell, Appl. Phys. Lett. 44 (1984) 1163−1164.

[53] M.A. Green, J.H. Zhao, A. H Wang, C.M. Chong, S. Narayanan, A.W. Blakers, S.R. Wenham, in: Proceedings of 8th European Communities Photovoltaics Solar Energy Conference, Riedel, Dordrecht, 1988, p. 164.

[54] A. H Wang, J.H. Zhao, M.A. Green, 24% efficient silicon solar cells, Appl. Phys. Lett. 57 (1990) 602−604.

[55] J.H. Zhao, A.H. Wang, M.A. Green, 24.5% efficiency silicon PERT cells on MCZ substrates and 24.7% efficiency PERL cells on FZ substrates, Prog. Photovolt. Res. Appl. 7 (1999) 471−474.

[56] J.H. Zhao, A.H. Wang, M.A. Green, Series resistance caused by the localized rear contact in high efficiency silicon solar cells, Sol. Energy Mater. Sol. Cells 32 (1994) 89−94.

[57] A.H. Wang, High Efficiency PERC and PERL Silicon Solar Cells, PhD Thesis, University of New South Wales, 1992, p. 111.

[58] A.G. Aberle, S.W. Glunz, A.W. Stephens, M.A. Green, High efficiency silicon solar cells: Si/SiO$_2$ interface parameters and their impact on device performance, Prog. Photovolt. Res. Appl. 2 (1994) 265−273.

[59] M.J. Kerr, A. Cuevas, Very low bulk and surface recombination in oxidized silicon wafers, Semicond. Sci. Technol. 17 (2002) 35.

[60] J.H. Zhao, A.H. Wang, M.A. Green, 24.5% efficiency PERT silicon solar cells on SEH MCZ substrates and cell performance on other SEH CZ and FZ substrates, Sol. Energy Mater. Sol. Cells 66 (2001) 27−36.

[61] M. Kunst, O. Abdallah, F. Wunsch, Passivation of silicon by silicon nitride films, Sol. Energy Mater. Sol. Cells 72 (2002) 335−341.

[62] B. Hoex, J. Schmidt, P. Pohl, M.C.M. van de Sanden, W.M.M. Kessels, Silicon surface passivation by atomic layer deposited Al$_2$O$_3$, J. Appl. Phys. 104 (2008), 044903-044903-12.

[63] V.A. Dao, J. Heo, Y. Kim, K. Kim, N. Lakshminarayan, J. Yi, Optimized surface passivation of n and p type silicon wafers using hydrogenated SiN$_x$ layers, J. Non-Crys. Solids 356 (2010) 2880−2883.

[64] B. Hoex, J. Schmidt, R. Bock, P.P. Altermatt, M.C.M. van de Sanden, W.M.M. Kessels, Excellent passivation of highly doped p-type Si surfaces by the negative-charge-dielectric Al$_2$O$_3$, Appl. Phys. Lett. 91 (2007) 4061.

[65] B. Hoex, S.B. S Heil, E. Langereis, M.C.M. van de Sanden, W.M.M. Kessels, Ultralow surface recombination of c-Si substrates passivated by plasma-assisted atomic layer deposited Al$_2$O$_3$, Appl. Phys. Lett. 89 (2006) 271.

[66] B. Hoex, J.J.H. Gielis, M.C.M.V. de Sanden, W.M.M. Kessels, On the c-Si surface passivation mechanism by the negative-charge-dielectric Al$_2$O$_3$, J. Appl. Phys. 104 (2008) 945.

[67] J. Benick, B. Hoex, M.C.M. van de Sanden, W.M.M. Kessels, O. Schultz, S.W. Glunz, High efficiency n-type Si solar cells on Al$_2$O$_3$-passivated boron emitters, Appl. Phys. Lett. 92 (2008) 4061.

[68] E. Schneiderlochner, R. Preu, R. Ludemann, S.W. Glunz, Laser-Fired rear contacts for crystalline silicon solar cells, Prog. Photovolt. Res. Appl. 10 (2010) 29−34.

[69] J.B. He, S. Hegedus, U. Das, Z. Shu, M. Bennett, L. Zhang, R. Birkmire, Laser-fired contact for n-type crystalline Si solar cells, Prog. Photovolt. Res. Appl. 23 (2015) 1091−1099.

[70] P.S. Liu, X.L. Zhang, L. Sun, S.S. Dai, C.H. Yu, X.D. Luo, Optimization of rear local Al-contacts on high efficiency commercial PERC solar cells with dot and line openings, J. Nanomater. 2014 (2014) 1−5.

[71] M. Hofmann, S. Janz, C. Schmidt, S. Kambor, D. Suwito, N. Kohn, J. Rentsch, R. Preu, S.W. Glunz, Recent developments in rear-surface passivation at Fraunhofer ISE, Sol. Energy Mater. Sol. Cells 93 (2009) 1074−1078.

[72] Z.R. Du, N. Palina, J. Chen, M.H. Hong, B. Hoex, Rear-side contact opening by laser ablation for industrial screen-printed aluminium local back surface field silicon wafer solar cells, Energy Procedia 25 (2012) 19−27.

[73] E. Urrejola, K. Peter, H. Plagwitz, G. Schubert, Al-Si alloy formation in narrow p-type Si contact areas for rear passivated solar cells, J. Appl. Phys. 107 (2010) 1363−1372.

[74] E. Urrejola, K. Peter, H. Plagwitz, G. Schubert, Silicon diffusion in aluminum for rear passivated solar cells, Appl, Phys. Lett. 98 (2011) 49−2564.

[75] S. Gatz, K. Bothe, J. Müller, T. Dullweber, R. Brendel, Analysis of local Al-doped back surface fields for high efficiency screen-printed solar cells, Energy Procedia 8 (2011) 318−323.

[76] X.B. Yang, J. Bullock, Q.Y. Bi, K. Weber, High efficiency n-type silicon solar cells featuring passivated contact to laser doped regions, Appl. Phys. Lett. 106 (2015) 471−474.

[77] H. Li, S.R. Wenham, Z.R. Shi, High efficiency PERL cells on CZ P-type crystalline silicon using a thermally stable a-Si: H/SiN$_x$, rear surface passivation stack, Sol. Energy Mater. Sol. Cells 117 (2013) 41−47.

[78] D. Lin, M. Abbott, P.H. Lu, B. Xiao, B. Hallam, B. Tjahjono, S. Wenham, Incorporation of deep laser doping to form the rear localized back surface field in high efficiency solar cells, Sol. Energy Mater. Sol. Cells 130 (2014) 83−90.

[79] E. Cornagliotti, A. Uruena, B. Hallam, L. Tous, R. Russell, F. Duerinckx, J. Szlufcik, Large area p-type PERL cells featuring local p+ BSF formed by laser processing of ALD Al$_2$O$_3$ layers, Sol. Energy Mater. Sol. Cells 138 (2015) 72−79.

[80] L. Tous, M. Aleman, R. Russell, E. Cornagliotti, P. Choulat, A. Uruena, S. Singh, J. John, F. Duerinckx, J. Poortmans, R. Mertens, Evaluation of advanced p-PERL and n-PERT large area silicon solar cells with 20.5% energy conversion efficiencies, Prog. Photovolt. Res. Appl. 23 (2015) 660−670.

[81] F. Feldmann, M. Bivour, C. Reichel, M. Hermle, S.W. Glunz, Passivated rear contacts for high-efficiency n-type Si solar cells providing high interface passivation quality and excellent transport characteristics, Sol. Energy Mater. Sol. Cells 120 (2014) 270−274.

[82] F. Feldmann, M. Bivour, C. Reichel, H. Steinkemper, M. Herm, S.W. Glunz, Tunnel oxide passivated contacts as an alternative to partial rear contacts, Sol. Energy Mater. Sol. Cells 131 (2014) 46−50.

[83] A. Moldovan, F. Feldmann, M. Zimmer, J. Rentsch, J. Benick, M. Hermle, Tunnel oxide passivated carrier-selective contacts based on ultra-thin SiO$_2$ layers, Sol. Energy Mater. Sol. Cells 142 (2015) 123−127.

[84] A. Richter, J. Benick, F. Feldmann, A. Fell, M. Hermle, S.W. Glunz, n-Type Si solar cells with passivating electron contact: identifying sources for efficiency limitations by wafer thickness and resistivity variation, Sol. Energy Mater. Sol. Cells 173 (2017) 96−105.

[85] W.C. Lee, C.M. Hu, Modeling CMOS tunneling currents through ultrathin gate oxide due to conduction -and valence-band electron and hole tunneling, IEEE Trans. Electron Devices 48 (2001) 1366−1373.

[86] F. Feldmann, M. Simon, M. Bivour, C. Reichel, M. Hermle, S.W. Glunz, Carrier-selective contacts for Si solar cells, Appl. Phys. Lett. 104 (2014) 1184.

[87] F. Feldmann, M. Simon, M. Bivour, C. Reichel, M. Hermle, S.W. Glunz, Efficient carrier-selective p- and n-contacts for Si solar cells, Sol. Energy Mater. Sol. Cells 131 (2014) 100−104.

[88] G.T. Yang, A. Ingenito, O. Isabella, M. Zeman, IBC c-Si solar cells based on ion-implanted poly-silicon passivating contacts, Sol. Energy Mater. Sol. Cells 158 (2016) 84−90.

[89] B. Nemeth, D.L. Young, M.R. Page, V. LaSalvia, S. Johnston, R. Reedy, P. Stradins, Polycrystalline silicon passivated tunneling contacts for high efficiency silicon solar cells, J. Mater. Res. 31 (2016) 671−681.

[90] A.S. Kale, W. Nemeth, S.P. Harvey, M. Page, D.L. Young, S. Agarwal, P. Stradins, Effect of silicon oxide thickness on polysilicon based passivated contacts for high-efficiency crystalline silicon solar cells, Sol. Energy Mater. Sol. Cells 185 (2018) 270−276.

[91] A. Rohatgi, B. Rounsaville, Y.W. Ok, A.M. Tam, F. Zimbardi, A.D. Upadhyaya, Y.G. Tao, K. Madani, A. Richter, J. Benick, M. Hermle, Fabrication and modeling of high-efficiency front junction n-type silicon solar cells with tunnel oxide passivating back contact, IEEE J. Photovolt. 7 (2017) 1236−1243.

[92] K. Tao, Q. Li, C.X. Hou, S. Jiang, J. Wang, R. Jia, Y. Sun, Y.T. Li, Z. Jin, X.Y. Liu, Application of a-Si/μc-Si hybrid layer in tunnel oxide passivated contact n-type silicon solar cells, Sol. Energy 144 (2017) 735−739.

[93] M. Taguchi, A. Yano, S. Tohoda, K. Matsuyama, Y. Nakamura, T. Nishiwaki, K. Fujita, E. Maruyama, 24.7% record efficiency HIT solar cell on thin silicon wafer, IEEE J. Photovolt. 4 (2014) 96−99.

[94] J.W. Shi, M. Boccard, Z. Holman, Plasma-initiated rehydrogenation of amorphous silicon to increase the temperature processing window of silicon heterojunction solar cells, Appl. Phys. Lett. 109 (2016) 1433–1435.

[95] D. Adachi, J.L. Hernandez, K. Yamamoto, Impact of carrier recombination on fill factor for large area heterojunction crystalline silicon solar cell with 25.1% efficiency, Appl. Phys. Lett. 107 (2015) 73–812.

[96] Z. Mrazkova, I.P. Sobkowicz, M. Foldyna, K. Postava, I. Florea, J. Pistora, P.R.I. Cabarrocas, Optical properties and performance of pyramidal texture silicon heterojunction solar cells: key role of vertex angles, Prog. Photovolt. Res. Appl. 26 (2018) 369–376.

[97] W. Kern, D. Puotinen, Cleaning solutions based on hydrogen peroxide for use in silicon semiconductor technology, RCA Rev. 31 (1970) 187–206.

[98] S. De Wolf, M. Kondo, Nature of doped a-Si: H/c-Si interface recombination, J. Appl. Phys. 105 (2009) 1211–1214.

[99] S. De Wolf, M. Kondo, Boron-doped a-Si: H/c-Si interface passivation: degradation mechanism, Appl. Phys. Lett. 91 (2007) 1211.

[100] R. Saive, A.M. Borsuk, H.S. Emmer, C.R. Bukowsky, J.V. Lloyd, S. Yalamanchili, H.A. Atwater, Effectively transparent front contacts for optoelectronic devices, Adv. Opt. Mater. 4 (2016) 1470–1474.

[101] T.F. Schulze, H.N. Beushausen, C. Leendertz, A. Dobrich, B. Rech, L. Korte, Interplay of amorphous silicon disorder and hydrogen content with interface defects in amorphous/crystalline silicon heterojunctions, Appl. Phys. Lett. 96 (2010) 670.

[102] A. Descoeudres, L. Barraud, R. Bartlome, G. Choong, S. De Wolf, F. Zicarelli, C. Ballif, The silane depletion fraction as an indicator for the amorphous/crystalline silicon interface passivation quality, Appl. Phys. Lett. 97 (2010) 503.

[103] S. De Wolf, M. Kondo, Abruptness of a-Si: H/c-Si interface revealed by carrier lifetime measurements, Appl. Phys. Lett. 90 (2007) 1012.

[104] H. Fujiwara, M. Kondo, Impact of epitaxial growth at the heterointerface of a-Si: H/c-Si solar cells, Appl. Phys. Lett. 90 (2007), 013503.

[105] S.K. Kim, J.C. Lee, S.J. Park, Y.J. Kim, K.H. Yoon, Effect of hydrogen dilution on intrinsic a-Si: H layer between emitter and Si wafer in silicon heterojunction solar cell, Sol. Energy Mater. Sol. Cells 92 (2008) 298–301.

[106] J. Ge, Z.P. Ling, J. Wong, R. Stangl, A.G. Aberle, T. Mueller, Analysis of intrinsic hydrogenated amorphous silicon passivation layer growth for use in heterojunction silicon wafer solar cells by optical emission spectroscopy, J. Appl. Phys. 113 (2013) 1690.

[107] A. Descoeudres, L. Barraud, S. De Wolf, B. Strahm, D. Lachenal, C. Guerin, Z.C. Holman, F. Zicarelli, B. Demaurex, J. Seif, J. Holovsky, C. Ballif, Improved amorphous/crystalline silicon interface passivation by hydrogen plasma treatment, Appl. Phys. Lett. 99 (2011) 123506.

[108] M. Mews, T.F. Schulze, N. Mingirulli, L. Korte, Hydrogen plasma treatments for passivation of amorphous-crystalline silicon-heterojunctions on surfaces promoting epitaxy, Appl. Phys. Lett. 102 (2013) 18–879.

[109] L.P. Zhang, W.W. Guo, W.Z. Liu, J. Bao, J.N. Liu, J.H. Shi, F.Y. Meng, Z.X. Liu, Investigation of positive roles of hydrogen plasma treatment for interface passivation based on silicon heterojunction solar cells, J. Phys. D Appl. Phys. 49 (2016) 165305.

[110] T. Watahiki, T. Furuhata, T. Matsuura, T. Shinagawa, Y. Shirayanagi, T. Morioka, T. Hayashida, Y. Yuda, S. Kano, Y. Sakai, H. Tokioka, Y. Kusakabe, H. Fuchigami, Rear-emitter Si heterojunction solar cells with over 23% efficiency, Appl. Phys. Express 8 (2015), 021402.

[111] M. Bivour, S. Schroer, M. Hermle, S.W. Glunz, Silicon heterojunction rear emitter solar cells: less restrictions on the optoelectrical properties of front side TCOs, Sol. Energy Mater. Sol. Cells 122 (2014) 120–129.

[112] L. Mazzarella, S. Kirner, B. Stannowski, B.R.L. Korte, R. Schlatmann, Appl. Phys. Lett. 106 (2015), 023902.

[113] R.F. Chen, L.P. Zhang, W.Z. Liu, Z.P. Wu, F.Y. Meng, Z.X. Liu, Optimized n-type amorphous silicon window layers via hydrogen dilution for silicon heterojunction solar cells by catalytic chemical vapor deposition, J. Appl. Phys. 122 (2017) 125110.

[114] Y. Zhang, C. Yu, M. Yang, Y.C. He, L.R. Zhang, J.Y. Zhang, X.X. Xu, Y.Z. Zhang, X.M. Song, H. Yan, Optimization of the window layer in large area silicon heterojunction solar cells, RSC Adv. 7 (2017) 9258.

[115] L. Mazzarella, S. Kirner, O. Gabriel, Nanocrystalline silicon emitter optimization for Si-HJ solar cells: substrate selectivity and CO_2 plasma treatment effect, Phys. Status Solidi A 214 (2016) 1–7.

[116] L. Mazzarella, A.B. Morales-Vilches, M. Hendrichs, S. Kirner, L. Korte, R. Schlatmann, B. Stannowski, Nanocrystalline n-type silicon oxide front contacts for silicon heterojunction solar cells: photocurrent enhancement on planar and textured substrates, IEEE J. Photovolt. 8 (2018) 70–78.

[117] J.P. Mailoa, C.D. Bailie, E.C. Johlin, S. Kirner, L. Korte, R. Schlatmann, B. Stannowski, A 2-terminal perovskite/silicon multijunction solar cell enabled by a silicon tunnel junction, Appl. Phys. Lett. 106 (2015) 1477.

[118] J. Werner, A. Walter, E. Rucavado, S.J. Moon, D. Sacchetto, M. Rienaecker, R. Peibst, R. Brendel, X. Niquille, S. De Wolf, P. Loper, M. Morales-Masis, S. Nicolay, B. Niesen, C. Ballif, Zinc tin oxide as high-temperature stable recombination layer for mesoscopic perovskite/silicon monolithic tandem solar cells, Appl. Phys. Lett. 109 (2016) 233902.

[119] Y.L. Wu, D. Yan, J. Peng, T. Duong, Y.M. Wan, S.P. Phang, H.P. Shen, N.D. Wu, C. Barugkin, X. Fu, S. Surve, D. Grant, D. Walter, T.P. White, K.R. Catchpole, K.J. Weber, Monolithic perovskite/silicon-homojunction tandem solar cell with over 22% efficiency, Energy Environ. Sci. 10 (2017) 2472–2479.

[120] J.H. Zheng, C.F.J. Lau, H. Mehrvarz, F.J. Ma, Y.J. Jiang, X.F. Deng, A. Soeriyadi, J. Kim, M. Zhang, L. Hu, X. Cui, D.S. Lee, J.M. Bing, Y. Cho, C. Chen, M.A. Green, S.J. Huang, A.W.Y. Ho-Baillie, Large area efficient interface layer free monolithic perovskite/homo-junction-silicon tandem solar cell with over 20% efficiency, Energy Environ. Sci. 11 (2018) 2432–2443.

[121] J.H. Zheng, H. Mehrvarz, F. J Ma, C.F.J. Lau, M.A. Green, S.J. Huang, A.W.Y. Ho-Baillie, 21.8% Efficient monolithic perovskite/homojunction-silicon tandem solar cell on 16 cm^2, ACS Energy Lett 3 (2018) 2299–2300.

[122] S. Albrecht, M. Saliba, J.P.C. Baena, F. Lang, L. Kegelmann, M. Mews, L. Steier, A. Abate, J. Rappich, L. Korte, R. Schlatmann, M.K. Nazeeruddin, A. Hagfeldt, M. Gratzel, B. Rech, Monolithic perovskite/silicon-heterojunction tandem solar cells processed at low temperature, Energy Environ. Sci. 9 (2016) 81–88.

[123] J. Werner, C.H. Weng, A. Walter, L. Fesquet, J.P. Seif, S. De Wolf, B. Niesen, C. Ballif, Efficient monolithic perovskite/silicon tandem solar cell with cell area >1 cm^2, J. Phys. Chem. Lett. 7 (2016) 161–166.

[124] R.D. Fan, N. Zhou, L. Zhang, R. Yang, Y. Meng, L.W. Li, T. Guo, Y.H. Chen, Z.Q. Xu, G.H.J. Zheng, Y. Huang, L. Li, L. Qin, X.H. Qiu, Q. Chen, H.P. Zhou, Toward full solution processed perovskite/Si monolithic tandem solar device with PCE exceeding 20%, Sol. RRL 1 (2017) 1700149.

[125] S.J. Zhu, X. Yao, Q.S. Ren, C.C. Zheng, S.Z. Li, Y.P. Tong, B. Shi, S. Guo, L. Fan, H.Z. Ren, C.C. Wei, B.Z. Li, Y. Ding, Q. Huang, Y.L. Li, Y. Zhao, X.D. Zhang, Transparent electrode for monolithic perovskite/silicon-heterojunction two terminal tandem solar cells, Nano Energy 45 (2018) 280–286.

[126] S.J. Zhu, F.H. Hou, W. Huang, X. Yao, B. Shi, Q.S. Ren, J.F. Chen, L.L. Yan, S.C. An, Z.X. Zhou, H.Z. Ren, C.C. Wei, Q. Huang, Y.L. Li, G.F. Hou, X.L. Chen, Y. Ding, G.C. Wang, B.Z. Li, Y. Zhao, X.D. Zhang, Solvent engineering to balance light absorbance and transmittance in perovskite for tandem solar cells, Sol. RRL (2018) 1800176.

[127] Q.S. Ren, S.Z. Li, S.J. Zhu, H.Z. Ren, X. Yao, C.C. Wei, B.J. Yan, Y. Zhao, X.D. Zhang, High near-infrared wavelength response planar silicon-heterojunction solar cells, Sol. Energy Mater. Sol. Cells 185 (2018) 124–129.

[128] J. Werner, L. Barraud, A. Walter, M. Brauninger, F. Sahli, D. Sacchetto, N. Tetreault, B. Paviet-Salomon, S.J. Moon, C. Allebe, M. Despeisse, S. Nicolay, S. De Wolf, B. Niesen, C. Ballif, Efficient near-infrared-transparent perovskite solar cells enabling direct comparison of 4-terminal and monolithic perovskite/silicon tandem cells, ACS Energy Lett 1 (2016) 474–480.

[129] K.A. Bush, A.F. Palmstrom, Z.J. Yu, M. Boccard, R. Cheacharoen, J.P. Mailoa, D.P. McMeekin, R.L.Z. Hoye, C.D. Bailie, T. Leijtens, I.M. Peters, M.C. Minichetti, N. Rolston, R. Prasanna, S. Sofia, D. Harwood, W. Ma, F. Moghadam, H.J. Snaith, T. Buonassisi, Z.C. Holman, S.F. Bent, M.D. McGehee, 23.6%-efficient monolithic perovskite/silicon tandem solar cells with improved stability, Nat. Energy 2 (2017) 17009.

[130] B. Chen, Z.S. Yu, K. Liu, X.P. Zheng, Y. Liu, J.W. Shi, D. Spronk, P.N. Rudd, Z. Holman, J.S. Huang, Grain engineering for perovskite/silicon monolithic tandem solar cells with efficiency of 25.4%, Joule 3 (2019) 177–190.

[131] F. Sahli, B.A. Kamino, J. Werner, M. Brauninger, B. Paviet-Salomon, L. Barraud, R. Monnard, J.P. Seif, A. Tomasi, Q. Jeangros, A. Hessler-Wyser, S. De Wolf, M. Despeisse, S. Nicolay, B. Niesen, C. Ballif, Improved optics in monolithic perovskite/silicon tandem solar cells with a nanocrystalline silicon recombination junction, Adv. Energy Mater. 8 (2017) 1701609.

[132] L. Mazzarella, Y.H. Lin, S. Kirner, M. Jost, L. Korte, S. Albrecht, R. Schlatmann, B. Stannowski, Infrared light management using a nanocrystalline silicon oxide interlayer in monolithic perovskite/silicon heterojunction tandem solar cells with efficiency above 25%, Adv. Energy Mater. 26 (2019) A487–A497.

[133] B.W. Schneider, N.N. Lal, M. Baker-Finch, T.P. White, Pyramidal surface textures for light trapping and antireflection in perovskite-on-silicon tandem solar cells, Opt. Express 22 (2014) A1422–A1430.

[134] R. Santbergen, R. Mishima, T. Meguro, M. Hino, H. Uzu, J. Blanker, K. Yamamoto, M. Zeman, Minimizing optical losses in monolithic perovskite/c-Si tandem solar cells with a flat top cell, Opt. Express 24 (2016) A1288.

[135] F. Sahli, J. Werner, B.A. Kamino, M. Brauninger, R. Monnard, B. Paviet-Salomon, L. Barraud, L. Ding, J.J.D. Leon, D. Sacchetto, G. Cattaneo, M. Despeisse, M. Boccard, S. Nicolay, Q. Jeangros, B. Niesen, C. Ballif, Fully textured monolithic perovskite/silicon tandem solar cells with 25.2% power conversion efficiency, Nat. Mater. 17 (2018) 820–826.

[136] K.A. Bush, S. Manzoor, K. Frohna, Z.J. Yu, J.A. Raiford, A.F. Palmstrom, H.P. Wang, R. Prasanna, S.F. Bent, Z.C. Holman, M.D. McGehee, Minimizing current and voltage losses to reach 25% efficient monolithic two-terminal perovskite-silicon tandem solar cells, ACS Energy Lett 3 (2018) 2173–2180.

[137] M. Jost, E. Kohnen, A.B. Morales-Vilches, B. Lipovsek, K. Jager, B. Macco, A. Al-Ashouri, J. Krc, L. Korte, B. Rech, R. Schlatmann, M. Topic, B. Stannowski, S. Albrecht, Textured interfaces in monolithic perovskite/silicon tandem solar cells: advanced light management for improved efficiency and energy yield, Energy Environ. Sci. 11 (2018) 3511–3523.

[138] E. Kohnen, M. Jost, A.B. Morales-Vilches, P. Tockhorn, A. Al-Ashouri, B. Macco, L. Kegelmann, L. Korte, B. Rech, R. Schlatmann, B. Stannowski, S. Albrecht, Highly efficient monolithic perovskite silicon tandem solar cells: analyzing the influence of current mismatch on device performance, Sust. Energ. Fuels 3 (2019) 1995–2005.

[139] E. Crossland, N. Noel, V. Sivaram, T. Leijtens, J.A. Alexander-Webber, H.J. Snaith, Mesoporous TiO_2 single crystals delivering enhanced mobility and optoelectronic device performance, Nature 495 (2013) 215–219.

[140] K. Eom, U. Kwon, S.S. Kalanur, H.J. Park, H. Seo, Depth-resolved band alignments of perovskite solar cells with significant interfacial effects, J. Mater. Chem. 5 (2017) 2563–2571.

[141] B. Chen, M.J. Yang, X.J. Zheng, C.C. Wu, W.L. Li, Y.K. Yan, J. Bisquert, G. Garcia-Belmonte, K. Zhu, S. Priya, Impact of capacitive effect and ion migration on the hysteretic behavior of perovskite solar cells, J. Phys. Chem. Lett. 6 (2015) 4693–4700.

[142] Z.G. Xiao, Y.B. Yuan, Y.C. Shao, Q. Wang, Q.F. Dong, C. Bi, P. Sharma, A. Gruverman, J.S. Huang, Giant switchable photovoltaic effect in organo-metal trihalide perovskite devices, Nat. Mater. 14 (2014) 193–198.

[143] Y. Bai, X.Y. Meng, S.H. Yang, Interface engineering for highly efficient and stable planar p-i-n perovskite solar cells, Adv. Energy Mater. 8 (2017) 1701883.

[144] T.H. Liu, K. Chen, Q. Hu, R. Zhu, Q.H. Gong, Inverted perovskite solar cells: progresses and perspectives, Adv. Energy Mater. 6 (2016).

[145] Y. Dong, Y. Ruixia, W. Kai, C.C. Wu, X.J. Zhu, J.S. Feng, X.D. Ren, G.J. Fang, S. Priya, S.Z. Liu, High efficiency planar-type perovskite solar cells with negligible hysteresis using EDTA-complexed SnO_2, Nat. Commun. 9 (2018) 3239.

[146] H.R. Tan, F.L. Chen, M.Y. Wei, Y.C. Zhao, M.I. Saidaminov, P. Todorovic, D. Broberg, G. Walters, F.R. Tan, T.T. Zhuang, B. Sun, Z.Q. Liang, H.F. Yuan, E. Fron, J. Kim, Z.Y. Yang, O. Voznyy, M. Asta, E.H. Sargent, Dipolar cations confer defect tolerance in wide-bandgap metal halide perovskites, Nat. Commun. 9 (2018) 1–10.

[147] Z. Yu, M. Leilaeioun, Z. Holman, Selecting tandem partners for silicon solar cells, Nat. Energ. 1 (2016) 16137.

[148] W.E. Mcmahon, K.E. Emery, D.J. Friedman, L. Ottoson, M.S. Young, J.S. Ward, C.M. Kramer, A. Duda, S. Kurtz, Fill factor as a probe of current-matching for $GaInP_2$/GaAs tandem cells in a concentrator system during outdoor operation, Prog. Photovolt. Res. Appl. 16 (2008) 213–224.

[149] U. Wurfel, D. Neher, A. Spies, S. Albrecht, Impact of charge transport on current–voltage characteristics and power-conversion efficiency of organic solar cells, Nat. Commun. 6 (2015) 6951.

[150] S. Albrecht, M. Saliba, J.P. Correa-Baena, K. Jager, L. Korte, A. Hagfeldt, M. Gratzel, B. Rech, Towards optical optimization of planar monolithic perovskite/silicon-heterojunction tandem solar cells, J. Opt. 18 (2016), 064012.

[151] B.F. Liu, L.S. Bai, Z. Chen, X.D. Zhang, D.K. Zhang, J. Ni, Q. Huang, C.C. Wei, J. Sun, X.L. Chen, H.Z. Ren, G.F. Hou, G.C. Wang, Y. Zhao, High efficiency triple junction thin film silicon solar cells with optimized electrical structure, Prog. Photovolt. Res. Appl. 23 (2015) 1313–1322.

[152] L.X. Meng, Y.M. Zhang, X.J. Wan, C.X. Li, X. Zhang, Y.B. Wang, X. Ke, Z. Xiao, L.M. Ding, R.X. Xia, H.L. Yip, Y. Cao, Y.S. Chen, Organic and solution-processed tandem solar cells with 17.3% efficiency, Science 361 (2018) 1094–1098.

[153] S.C. Chen, Q.D. Zheng, Z.G. Yin, D.D. Cai, Y.L. Ma, High performance thermal-treatment-free tandem polymer solar cells with high fill factors, Org. Electron. 47 (2017) 79–84.